

Morphologies and Central Stars of Planetary Nebulae in the Galactic bulge from VLT, *HST* and Pan-STARRS imaging

Shuyu Tan,^{1,2*} Quentin A. Parker^{1,2†} Albert Zijlstra^{3,2,1} Andreas Ritter^{1,2}

¹*Department of Physics, Chong Yuet Ming Physics Building, The University of Hong Kong, Pokfulam Road, Hong Kong*

²*The Laboratory for Space Research, The University of Hong Kong, Cyberport 4, Hong Kong*

³*Jodrell Bank Centre for Astrophysics, The University of Manchester, Oxford Road, M13 9PL, Manchester, UK*

Accepted XXX. Received YYY; in original form ZZZ

ABSTRACT

This is the first in a series of papers that present sets of different results for 136 compact, known planetary nebulae within a 10×10 degree region of the Galactic bulge. We use a large, previously unpublished sample of our own extensive ESO 8 m VLT deep imaging and spectroscopic data. This is combined with archival deep *HST* imaging where available to provide a detailed morphological classification and study. The influence of angular resolution and sensitivity when assigning a morphology is discussed. A large fraction (68%) of the sample are shown to be bipolars and the implications for this in the context of planetary nebulae progenitors are explored. Four new planetary nebula central stars are also identified which are not in *Gaia*. This is based on both VLT and deep archival Pan-STARRS broad-band imagery. Some 11 putative central stars previously reported, based on *Gaia* positions, are also not the true central star. In other cases the *Gaia* central stars reported in the literature are actually based on the overall centroid position of a very compact planetary nebula rather than the actual central star within it. *Gaia* parallax distances and kinematic ages for PNe in this sample are provided where possible based on fresh angular size measures from the new VLT imagery and *Gaia* distances and literature expansion velocities when available. All these results are discussed within the context of the overall characteristics of the Galactic bulge and its planetary nebula population.

Key words: planetary nebulae: general – Galaxy: bulge – Galaxy: centre

1 INTRODUCTION

Planetary nebulae (PNe) are bright, gaseous emission envelopes ejected by low- to intermediate-mass stars ($M_{\star} \sim 0.8 - 8M_{\odot}$) during their post-AGB stage as the residual cores evolve to the white dwarf (WD) phase. Most PNe with hotter ($> 45,000\text{K}$) central stars (CSPN) are optically thin to Lyman continuum photons (e.g. Schönberner et al. 2007). As such, outermost electrons of multiply-charged ions are ejected, giving PNe their predominate and strong emission lines. This makes PNe detectable even at large Galactocentric distances and in external galaxies like the Magellanic clouds (Reid & Parker 2006) and other members of the local group (e.g. Jacoby 1980; Merrett et al. 2006). For an excellent, recent, general PNe review see Kwitter & Henry (2022) and for a more specific PNe discovery and selection techniques review see Parker (2022a).

PNe exhibit a diversity of shapes (morphologies hereafter) that nevertheless can be allocated to a few basic underlying forms: elliptical (E), round (R), bipolar or butterfly (B), in rare cases irregular (I), asymmetric (A) and, when extremely compact, (S) for point-source like (see, e.g. Greig 1971; Chu et al. 1987; Machado et al. 2000; Stanghellini et al. 2002a; Corradi et al. 2003; Parker et al. 2006; Sahai et al. 2011a).

Current morphological classifications assigned to all known

Galactic PNe are contained in the "Gold Standard" HASH database¹ Parker et al. (2016). HASH consolidates and federates available multi-wavelength imaging, spectroscopic and other data for both Galactic and Magellanic Cloud PNe. The assigned morphologies adopt the ERBIAS/sparm classification scheme introduced by Parker et al. (2006) and used exclusively in HASH. The underlying physical causes for the observed morphological variety and their connection to their central stars (CSPN hereafter) have been extensively explored (e.g. Stanghellini et al. 2002a), but mysteries concerning the definitive shaping mechanisms remain.

From an observational perspective, the interpretation of PN shapes has been largely dependent on the morphological characterisation of 2-D projections of largely optical emission distributions from what are obviously 3-D nebula sources. The conversion from 2-D to a true 3-D representation of a PN depends on detailed kinematic sampling from high dispersion Integral Field Unit (IFU) spectroscopic observations (e.g. Danehkar et al. 2013) and associated 3-D modelling with software such as SHAPE (Steffen & López 2006; Clyne et al. 2015). While IFU observations are now becoming more common, e.g. Ali et al. (2016); Clairmont et al. (2022), they remain, for now, the exception. This is at least partly due to the competition for access to limited, suitable IFU instrumentation (i.e. those with sufficient areal coverage, and angular and kinematic resolution). Consequently, morphological classifications and more fundamentally an understanding

* E-mail: shuyut@hku.hk

† E-mail: quentinp@hku.hk

¹ HASH: available online <http://www.hashpn.space>

of them, is based on PNe 2-D imagery that will remain the default for the foreseeable future.

Modern, higher sensitivity and higher angular resolution observations, using dedicated ground-based and space-based telescopes and surveys, have further revealed a wealth of additional small-scale and large-scale features beyond the basic forms. These have further complicated this basic classification scheme. They include point-symmetric structures, jets, ansae, minor bipolar and multi-polar lobes, internal nebular striations, external, concentric rings and extensive "AGB" haloes and shells, (e.g. [Górny et al. 1999](#); [Sahai et al. 2011b](#); [Sabin et al. 2014](#); [Akras & Gonçalves 2016](#); [Stanghellini et al. 2016](#); [Sabin et al. 2021](#)). These secondary morphological features are classified by the "sparm" system used by HASH (see later).

Some background to the importance of PNe morphologies is given in Section 2. The observations yielding the PN imaging data and details of the morphological and CSPN analysis are described in Section 3 and Section 4 respectively. The various measurement results with the imaging data are listed and discussed in Section 5. In Section 6, we briefly summarise current ideas about PN shaping mechanisms and compare the properties of PNe in our sample with theoretical predictions. Finally, Section 7 contains a summary of our main results with an emphasis on the prevalence of bipolar PNe uncovered.

2 WHY ARE PNE MORPHOLOGIES IMPORTANT?

PNe morphologies are a useful means to describe how gaseous ejected shells of dying stars are manifested. The most accurately determined morphologies from the best available (usually optical) imagery can permit detailed investigation as a function of different parameters. This is especially when combined with the statistical power from HASH classifications of large numbers of PNe. Such parameters include Galactic location and environment, angular/physical size (so evolution), CSPN properties when available (including if in a binary system), nebular abundances and kinematic ages etc. Such studies can provide vital clues into the actual shaping mechanisms at play and their relative importance.

Indeed, PNe morphologies, as a key component of multi-wavelength and spectroscopic observation and analysis, can deliver powerful insights into their chemical and physical conditions, central star and nebula evolutionary stages and other key properties. PNe morphologies can reveal effects from interactions with the local ISM, e.g. [Wareing et al. \(2007\)](#), the influence of possible external or internal magnetic fields, e.g. [Sabin et al. \(2007\)](#), the results of fast winds interacting with previously ejected material at an earlier stage of evolution, e.g. [Kastner et al. \(2022\)](#) and, as often invoked, the influence of CSPN binarity and common envelope evolution as perhaps the key driver of PNe shaping, e.g. [De Marco \(2009a\)](#).

Being so diverse, PNe shapes are clearly telling us something fundamental about how and why PNe are formed and why most are not just a canonical, spherical gaseous envelope ejected from a single star. The observed diversity may result, at least in part, from different types of progenitor stars where the basic 3 main bipolar, elliptical and round PNe morphologies are suggested to emerge from stars that have slightly different mass distributions ([Górny et al. 1997](#)) and where bipolar PNe in particular are thought produced by more massive progenitors ([Corradi & Schwarz 1995](#); [Mellema 1997](#); [Zhang & Kwok 1998](#); [Phillips 2001](#)). This is especially given their preferred location at lower Galactic scale-heights in the mid-plane ([Parker et al. 2006](#)). Here, any PNe found in such assumed younger environments should have derived from higher mass stars to be going through the

PN phase now. Also see [Stanghellini et al. \(1993\)](#); [Amnuel \(1995\)](#); [Greig \(1971\)](#); [Górny et al. \(1997\)](#); [Stanghellini et al. \(2002b\)](#) for further detailed comment and see [Balick & Frank \(2002\)](#) for a review. Indeed, non-spherical features observed in the majority of PNe (~80% - as determined from HASH) have long been attributed to stellar or sub-stellar companions. See [De Marco \(2009a\)](#) for a detailed case and review of the "binary hypotheses" of PNe formation and the supposition that most bipolar PNe arise from binaries ([Soker 1998](#)). This counterpoint to the high mass, young progenitor bipolar origin scenario was addressed by this latter work. Here, it is suggested that the observed correlation of more massive progenitors with bipolar PNe is due to larger ratios of the physical radii of red giant branch (RGB) stars compared to AGB stars that is exhibited by lower-mass stars compared to their higher mass equivalents. The larger radii of such stars on the RGB cause most stellar binary companions to interact with their lower-mass primaries that are already on the RGB. These could have formed bipolar PNe if the primary had been on the AGB.

2.1 The importance of PNe in the Galactic bulge

The Galactic bulge has been considered as an almost separate entity to the rest of the Galaxy consisting largely of older stars (~10 Gyrs) and low in gas and dust. For a good review see [Nataf \(2016\)](#). Previously, the bulge has been considered like an elliptical galaxy in overall colour and form. This simple picture has changed considerably over the last 20 years and the long-held view that the bulge is shaped like a tri-axial spheroid composed of old stars ([Dwek et al. 1995](#)), resembling an elliptical Galaxy shorn of its disk and spiral arms, is no longer valid. The bulge is now known to host an elongated central bar ([Blitz & Spergel 1991](#); [Stanek et al. 1997](#)). A detailed 3-D map using red clump stars as distance indicators (by assuming they have a constant absolute magnitude) also showed the bulge to be X-shaped ([Saito et al. 2011, 2012a](#); [Wegg & Gerhard 2013](#)), i.e. a boxy peanut-shaped structure that becomes a bar in the inner bulge (e.g. [Athanasoula 2005](#); [Zoccali et al. 2014](#)) which has implications for feasible formation scenarios. Bulge dynamics are different to the plane and in the inner region more chaotic.

How well the currently available bulge PNe sample represents the underlying stellar population and its evolutionary history remains an open question. However, PNe represent a highly visible "touchstone" population from which to investigate certain bulge characteristics (e.g. [Peimbert 1978](#); [Peimbert & Torres-Peimbert 1983](#); [Corradi & Schwarz 1995](#)). Their range of inherent morphologies may play a significant role in aiding understanding late stage stellar evolution mass loss processes and, via spectroscopy of the ejecta of different PNe types, large-scale chemical evolution and trends ([Bensby et al. 2013, 2017](#)). This provides a key motivation for our work. The reliable morphological classification for compact Galactic bulge PNe, identification of their CSPN and estimation of their kinematic ages are the main focus of this first paper.

3 SAMPLE SELECTION: NEW OBSERVATIONS AND ARCHIVAL DATA

In this work we present results from our new ESO VLT narrow-band imagery for PNe located in the inner 10×10 degree region of the Galactic bulge. All the targets observed by the ESO VLT and in the *HST* samples were selected to be highly likely physical members of the bulge. This is based on the following criteria as detailed in

Rees & Zijlstra (2013) and designed to reject contamination from bulge stars and foreground objects.

- (i) The PN lies within the inner 10 degrees of the Galactic Centre.
- (ii) The PN has a measured angular size of > 2 arcseconds and less than 35 arcseconds; e.g. see Acker et al. (2006) that was further restricted to ≤ 10 arcseconds (see below)
- (iii) When a 5 GHz PN radio flux is available it must lie within the interval (4.2 mJy, 59.1 mJy). (Siódmiak & Tylenda 2001; Acker et al. 1992)

Whether a bulge PNe is compact or extended is irrelevant to their ages given the short overall PNe lifetimes c.f. that of their host stars. However, it is germane to their nebular evolutionary state and ease of observation. The further restriction of the above selection criteria to angular extents ≤ 10 arcseconds was applied to: i) yield young PNe that are usually of higher surface brightness; ii) be less affected by any seeing variations while iii) producing a sample size for the VLT that has realistic prospects of full completion. The restricted angular size also makes the sample more amenable to deep spectroscopy for detailed abundance studies - a key aim of this overall project. Their compactness, though, does make their morphologies harder to discern from existing ground based imagery. Here we re-examine both existing *Hubble Space Telescope* (HST) and our new VLT imagery to provide significantly improved classifications.

The above final sample selection was based on vetting of all confirmed PNe from HASH in the bulge region that satisfied the above original criteria back in 2015. This produced 136 sources. However, HASH is an evolving database and in the interim many PNe entries have been updated, including some angular size measurements. Indeed, we provide fresh angular size measurements for all PNe in this sample (refer section 5.1) based largely on the new VLT narrow-band imagery. As a result many PNe would no longer satisfy the strict ≤ 10 arcsecond diameter criterion. Many are now a little larger in these fresh estimates with an average value of 9.5 arcseconds with $\sigma = 4.2$, but the integrity of the sample as compact PNe in the Galactic bulge remains.

All 136 original targets were spectroscopically observed with the FORS2 instrument mounted on UT1 (Antu) of the European Southern Observatory (ESO) 8.2 m Very Large Telescope (VLT) (Appenzeller et al. 1998). The observations took place between 2015 and 2019 under program IDs 095.D-0270(A), 097.D-0024(A), 099.D-0163(A), and 0101.D-0192(A) for PIs Zijlstra and Parker. FORS2 narrow-band pre-imaging was obtained for all 136 sources. This imagery was supplemented by a further 40 objects previously observed using the Wide Field and Planetary Camera 2 Instrument (WFPC2) of the HST in 2002, 2003 and 2009 through HST-SNAP-8345 (PI: Sahai), HST-SNAP-9356 (PI: Zijlstra) and HST-GO-11185 (PI: Rubin). HST imagery was used for morphological classification whenever available as it is obviously far superior.

The main point of the VLT observations was to obtain deep, high quality PNe spectroscopy for abundance studies (the subject of 3 further papers in this series). The generally excellent narrow-band VLT imaging obtained for most was a mere by-product of the FORS2 spectroscopic observational process that often requires pre-imaging of the PNe in order to determine where best to place the spectroscopic slit. The final observed VLT sample here comprises 136 PNe, representing about $\sim 20\%$ of the currently known bulge PNe population in HASH.

Our completed ESO VLT project was designated as a filler programme with no photometric quality requirement (and one of the reasons for choosing the target sample to be ≤ 10 arcseconds across). These could proceed even under modest conditions, e.g. some clouds

and/or high humidity and/or relatively poor seeing. This gave increased likelihood of our observations being obtained but as a result care must be taken when attempting any reliable photometric assessment. Fortunately, for the purposes of this particular paper, the adverse effects on discernable morphological detail and point source (CSPN) detection were modest over the range of observing conditions achieved in practice.

Our VLT imagery and a careful assessment of the existing HST imagery now enables us to better resolve both macro- and microscopic structures for most of the objects not seen in previous studies and so present fresh, detailed morphological classification and analysis of this sample. These data are combined with the excellent resolution and deep Pan-STARRS broad band imagery (Kaiser et al. 2010), when available. This includes the key blue 'g-band' and has allowed more accurate measurements and improvement to the position and information of CSPN where they are clearly identifiable, including 4 new CSPN discoveries not in *Gaia*.

3.1 The ESO VLT instrumental configuration

The FORS2 instrument is a multi-mode optical instrument mounted on the ESO VLT UT1 telescope at the Cassegrain focus. It can perform imaging and long slit spectroscopy but also has a multi-object spectroscopy capability and even polarimetry (Nicklas et al. 1997) that can cover a wavelength range from the atmospheric cut-off in the blue out to $\sim 1\mu\text{m}$ in the red.

FORS2 is equipped with a mosaic of two MIT CCD detectors, each a 4096×2048 pixel array with an image scale of 0.126 arcsec/pixel (see FORS2 manual²). So called "pre-imaging" observations were performed under the direct imaging mode (IMG) using two narrow-band filters, $H\alpha$ (FWHM of 61\AA at 6563\AA , transmits both $H\alpha$ and [N II] $\lambda\lambda$ 6548, 6584 lines) and [O III] (FWHM of 57\AA at 5001\AA). Among the 136 confirmed PNe, 83 PNe have images with both $H\alpha$ and [O III] filters. A further 26 PNe have an image with the $H\alpha$ filter only and 27 have an image with the [O III] filter only. The integration times vary from 2 seconds for the high surface brightness PNe to 240 seconds for those of lower surface brightness. Despite the filler program status the recorded seeing was typically better than 1.5 arcseconds, underlining the excellent nature of the ESO VLT site. A summary log of the VLT observations is provided in Table A1 in Appendix A. All images were bias-subtracted and flat-fielded, where the associated raw calibration files are available, using the standard ESO Reflex Data Reduction Pipeline (Freudling et al. 2013).

3.2 The HST imagery

For the 40 HST sub-sample of bulge PNe, the WFPC2/HST has 800×800 pixel silicon CCD with a pixel size of 0.046 arcseconds. The narrow-band filter F656N (22\AA wide at 6564\AA) was utilised for all observations. Exposure times were mostly 80 or 120 seconds but a few were of 0.5, 40, 160, 200, 240, 320 and 400 seconds. The F502N filter (covering [O III] 5007\AA) was used for 31 objects in our sample. Here, the exposure time ranged from 60 to 600 seconds. The summary log of the HST observations is given in Table A2 in Appendix A. Due to the higher spatial resolution of the HST, these imaging data were used wherever possible for morphological classifications and for CSPN hunting and verification in this study.

² <http://www.eso.org/sci/facilities/paranal/instruments/fors/inst/pola.html>

3.3 Pan-STARRS imagery as a useful adjunct

For some PNe the narrow-band VLT imagery was less sharp and indeed less deep for continuum sources than the available broad-band Pan-STARRS imagery (Kaiser et al. 2010) due to occasional poorer seeing for our VLT filler program. Pan-STARRS is itself superior and better than the default main ~ 2 arcsecond resolution HASH imagery from the SuperCOSMOS $H\alpha$ survey (Parker et al. 2005) that was originally used for morphological classification and that does not work well for the compact PNe sample here. Pan-STARRS is also particularly useful for CSPN verification as the broad multi-band photometry is quite deep. The typical 5σ limiting magnitudes for point sources in the g, r, i, z and y bands are 23.3, 23.2, 23.1, 22.3 and 21.4 respectively (Chambers et al. 2016). This is much deeper than *Gaia*, especially for the g-band, and also allows CSPN candidate blue colours to be seen. This helps to confirm the CSPN identifications made here.

In Fig. 1 we provide two examples showing a comparison of the VLT (left) and Pan-STARRS (right) imagery. The image quality of the narrow-band VLT imagery is usually superior to that of Pan-STARRS. The upper panel present the images of PNG 007.5+07.4. The VLT image clearly shows a well defined ring structure and a faint AGB halo but not the CSPN which is only visible in the broad-band Pan-STARRS red image shown. It is also clear that Pan-STARRS goes deeper (in this example) for continuum sources than the VLT equivalent but with a slightly inferior stellar PSF. The lower panel contrasts images of PN 007.6+06.9 where the VLT image (left) exhibits a ring structure with an enhancement in brightness in the NW direction, as well as hints of an outer shell. The Pan-STARRS image (right) is superior to the VLT both in terms of detail and again the CSPN is only visible in the Pan-STARRS broad-band red image.

Although the two Pan-STARRS telescopes are only 1.8 m in diameter they benefit from generally excellent seeing conditions being situated at Haleakala Observatory, Hawaii. This yielded the high quality broad band filter images used here for both checking CSPN candidates and uncovering CSPN not evident in the VLT imaging. Often the VLT imaging does not go deep enough to detect faint CSPN in the narrow-band filters. Pan-STARRS data was only incorporated into HASH after original morphological classifications were assigned.

4 MORPHOLOGICAL CLASSIFICATION, CSPN AND OTHER MEASUREMENTS

Of the 136 PNe in our sample, imaging data of 96 PNe are taken from the VLT observations while observations of 40 are from the *HST* and used for morphological classification. The Galactic distribution of this sample is shown in Fig. 2. All spectroscopic data are used later in this series of papers for accurate abundance determinations and analysis (Tan et al., in preparation). The full set of the best available optical imagery for each of the 136 PNe is presented in Appendix B.

Below we provide details of the updated morphological classifications obtained from the *HST* and VLT imagery and the detection and positional measurements of any plausible CSPN seen in these and the supplementary Pan-STARRS images.

4.1 Morphological classification

As mentioned, the "ERBIAS sparm" morphological classification scheme, first described in Parker et al. (2006), was adopted. The upper case designator first indicates the basic class as Elliptical (E), Round

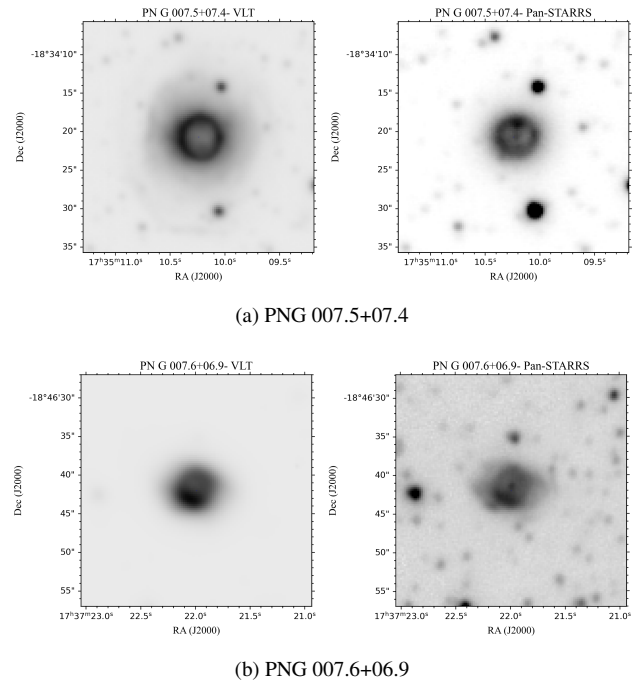


Figure 1. Two comparison examples between the VLT (left) and Pan-STARRS (right) imagery. The upper panel is of PNG 007.5+07.4. The CSPN is only visible in the broad-band red Pan-STARRS image. Pan-STARRS goes deeper in this example for continuum sources than the VLT equivalent. The lower panel contrasts images of PNG 007.6+06.9. The Pan-STARRS image (right) in this case is superior to the VLT both in terms of detail and depth. Again the CSPN is only visible in the Pan-STARRS broad-band red image.

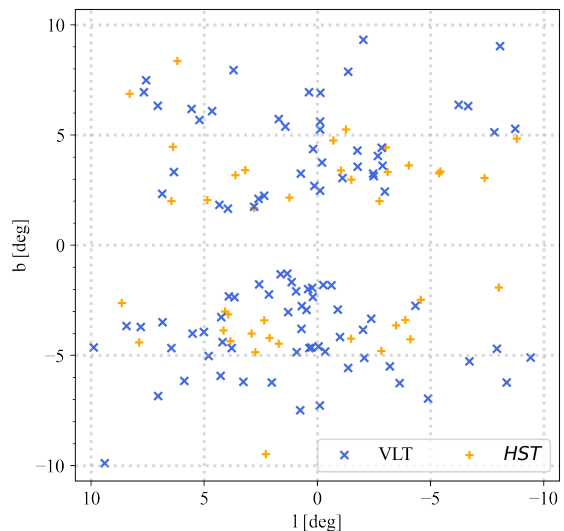


Figure 2. Distribution of the 136 bulge PNe sample observed with the VLT in a Galactic latitude versus Galactic longitude plot. The blue crosses mark the objects with no *HST* data so the best images are usually from the VLT observations. The orange crosses represent objects imaged with the *HST* (even if they also have VLT pre-imaging observations).

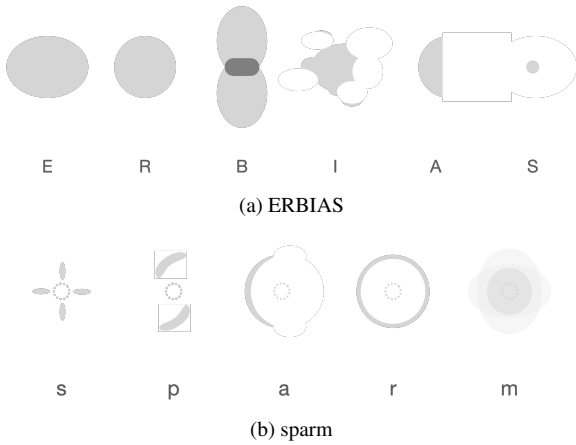


Figure 3. A schematic of the main classifiers ‘ERBIAS’ and the sub-classifiers ‘sparm’ for indicating the PN morphology taken from (Parker et al. 2006) and (Parker et al. 2016). The dotted circles indicating the centre of the nebula are used as a reference to infer the secondary PN morphological features.

(R), Bipolar (B), Irregular (I), Asymmetric (A) and the unresolved quasi-stellar PNe (S). To describe the secondary structural features evident in the nebulae, the lower-case ‘sparm’ sub-classifiers were used immediately following the main class. These are used to describe an object that also exhibits obvious internal structure with details such as filaments, knots, striations etc ‘s’, possesses some point symmetry ‘p’, has an enhancement or one-sided brightness/asymmetry ‘a’, has an evident, even if fractured, ring-like structure or annulus ‘r’ or shows multiple shells or external structure ‘m’. A scheme schematic of the main and sub-classifiers is presented in Fig. 3. PNe may have none, several or even all of these sub-classifiers.

This classification scheme was then applied to the best available multi-wavelength or single, narrow-band image data for all PNe in our sample, whether it be from the *HST* or VLT. Of course this is inevitably a somewhat subjective judgement but the team is very experienced.

In Table 1 we present the updated morphological classifications for all 136 PNe in the selected bulge sample. Provided are the unique HASH ID number, the PNG designation, remeasured PNe centroid positions in J2000 RA and DEC, our updated morphological classifications and new angular diameter estimates (in arcseconds) measured from the VLT, *HST* and, in three cases, Pan-STARRS imagery. The telescope used is indicated in the last entry for each PN.

4.2 Astrometric integrity of the *HST*, Pan-STARRS and VLT imagery

Prior to detection and measurement of any CSPN evident in our data and comparison with *Gaia* it is necessary to establish the astrometric integrity across the various image data sets used. The applied astrometric solution for the *HST* (Anderson & King 2000) and Pan-STARRS data (Magnier et al. 2020) are reported as highly accurate. However, for the VLT imagery the astrometric fits provided from the ESO pipelines are not sufficiently accurate. It was necessary to boot-strap the VLT data to the equivalent *Gaia* data co-ordinate system before CSPN position comparisons. Small-scale translation and rotations were needed with typical offsets found to be 1 to a few VLT image pixels. This task was accomplished using Python scripts after identifying 6-10 stars in common widely spread across the images and *Gaia* data.

We also noticed a small systematic ~ 1 pixel offset to the North

and the West between the *Gaia* and Pan-STARRS frames and so a similar exercise was done here. Once completed we could then confidently assess the CSPN detected in the VLT, *HST* and Pan-STARRS imagery with the co-ordinates for the CSPN reported from *Gaia* data, e.g. Chornay & Walton (2021) and González-Santamaría et al. (2021) (see later).

4.3 Identification of CSPN

CSPN exhibit a wide range of heterogeneous properties and range from weak emission line stars (wels) to PG1159 stars, Wolf-Rayet type stars of the [WO], [WC] and even [WN] sequence (where the square bracket demarcates them from their population I high mass equivalents), different kinds of white dwarfs (DA, DAO, DO) and early and late O(H) and Of(H) stars etc, e.g. see Weidmann et al. (2018). How these stars have influenced the characteristics of the surrounding PNe is a key question and it depends on the timescales for the CSPN evolution and the visibility lifetime of the PN itself as it expands to ultimate dissolution in the ambient ISM e.g. see Fragkou et al. (2022).

In Table 2 we present the results of our careful investigation into the CSPN that we have independently identified in the *HST*, and astrometrically corrected VLT and Pan-STARRS imagery for all 136 PNe in our sample.

A total of 78 PNe have high confidence CSPN detected in the combined imaging data for a 57.4% detection rate. In most cases (58/78) the *HST* and VLT imagery provided the best data to identify the CSPN. However, in 18 cases the Pan-STARRS data was the best (though in 2 cases the CSPN was seen only in the Vista Variables in the Via Lactea (VVV) Near Infrared survey data (Saito et al. 2012b) due to dust extinction. This is because not only is the Pan-STARRS data deeper in many cases than that from the VLT, but for some sources the resolution is also better (due to the filler program nature of the VLT observations). Also, because Pan-STARRS used broad-band filters, the CSPN (and their colours) are easier to see.

These candidates are selected as being almost exclusively at the exact geometric centres of their respective host, compact PNe. Of these, 22 are already listed in the putative CSPN catalogue of Weidmann et al. (2020) that reports not the actual accurate CSPN co-ordinates in many cases, but rather the centroid positions of these high surface brightness, compact PNe. These are quoted only to be accurate to 0.1 seconds of time for Right Ascension and 0.1 seconds of arc for Declination. This is insufficiently accurate for reporting the positions of the true CSPN visible in the *HST* and VLT imagery. The offsets of 0.20 to 0.5 arcseconds typical in both co-ordinates in Weidmann et al. (2020) can miss the CSPN completely in the high resolution imagery. The spectral types of 22 CSPN reported in Weidmann et al. (2020) are also shown in the last column. They largely comprise O-type stars, wels and [WR] stars.

Of our 78 CSPN, 74 also have *Gaia* EDR3 counterparts included in Table 2. We also provide *Gaia* CSPN G magnitudes, proper motions and distance estimates where available. An assessment of the reported *Gaia* CSPN identifications is given below.

5 RESULTS

Here we present results from our work on morphological classifications, CSPN identification and measurement and kinematic age estimates. PNe centroid positions, morphological classifications, updated angular size estimates, CSPN coordinates have been determined (where available) from the combined *HST*, VLT, Pan-STARRS

Table 1. Listing of HASH & PNG IDs, J2000 RA/DEC positions, morphological classifications, new, angular size measurements (arcseconds) for our PNe sample as measured from the VLT, *HST* imagery and, in 3 cases, from Pan-STARRS. The telescope data used is indicated as the last entry for each PN.

HASH ID	PN G	PN Centroid Coords.		Morph.	Ang. Diam.	Tele.	HASH ID	PN G	PN Centroid Coords.		Morph.	Ang. Diam.	Tele.
		RA(J2000)	DEC(J2000)						RA(J2000)	DEC(J2000)			
12	000.1+02.6	17:35:35.44	-27:24:05.37	Ars	12.6	VLT	171	005.8-06.1	18:22:54.20	-26:49:17.00	Bms	9.4	VLT
16	000.1+04.3	17:29:23.41	-26:26:04.38	B	12.0	VLT	4108	006.1+08.3	17:28:57.61	-19:15:53.95	Ems	2.4	<i>HST</i>
17	000.1-02.3	17:55:20.53	-29:57:36.78	Rars	10.2	VLT	179	006.3+03.3	17:47:33.95	-21:47:23.71	Bams	9.0	PS
19	000.2-01.9	17:53:45.64	-29:43:46.98	Brs	19.4	VLT	180	006.3+04.4	17:43:28.75	-21:09:51.77	Bamps	5.4	<i>HST</i>
20	000.2-04.6	18:04:44.09	-31:02:48.88	Bs	8.0	VLT	182	006.4+02.0	17:52:41.44	-22:21:57.18	Bmps	7.0	<i>HST</i>
24	000.3+06.9	17:20:22.04	-24:51:52.24	Brs	11.0	VLT	181	006.4-04.6	18:18:13.33	-25:38:07.95	Eas	9.2	VLT
22	000.3-04.6	18:05:02.68	-30:58:18.03	Bms	11.8	VLT	189	006.8+02.3	17:52:22.62	-21:51:13.51	Bms	5.2	VLT
26	000.4-01.9	17:54:25.37	-29:36:08.89	Brs	8.4	VLT	188	006.8-03.4	18:14:28.74	-24:43:38.12	Bms	7.0	VLT
27	000.4-02.9	17:58:19.40	-30:00:39.36	Bamrs	8.8	VLT	193	007.0+06.3	17:38:11.54	-19:37:35.83	Bps	7.2	VLT
40	000.7+03.2	17:34:54.72	-26:35:57.36	Bprs	17.8	VLT	192	007.0-06.8	18:27:59.62	-26:06:48.11	Bms	12.4	VLT
37	000.7-02.7	17:58:09.59	-29:44:19.98	Bps	8.2	VLT	197	007.5+07.4	17:35:10.24	-18:34:20.71	Eamrs	18.2	PS
38	000.7-03.7	18:02:19.26	-30:14:25.94	Bmrs	11.4	VLT	198	007.6+06.9	17:37:21.99	-18:46:42.00	Bamrs	16.6	PS
42	000.7-07.4	18:17:37.20	-31:56:46.68	Ears	11.8	VLT	200	007.8-03.7	18:17:16.01	-23:58:55.07	Bams	17.0	VLT
50	000.9-02.0	17:56:02.79	-29:11:16.69	Bps	5.2	VLT	201	007.8-04.4	18:20:08.84	-24:15:05.39	Eamrs	7.2	<i>HST</i>
48	000.9-04.8	18:07:06.16	-30:34:17.39	Eamrs	15.4	VLT	4111	008.2+06.8	17:38:57.37	-18:17:35.92	Bms	4.8	<i>HST</i>
54	001.1-01.6	17:54:52.07	-28:48:55.79	Eam	7.8	VLT	208	008.4-03.6	18:18:23.81	-23:24:57.50	Bmprs	25.2	VLT
58	001.2+02.1	17:40:12.83	-26:44:21.83	Bamrs	5.2	<i>HST</i>	210	008.6-02.6	18:14:50.91	-22:43:55.52	Bams	4.2	<i>HST</i>
60	001.2-03.0	18:00:37.62	-29:21:50.78	E	6.6	VLT	217	009.4-09.8	18:44:43.15	-25:21:34.06	Eamrs	8.4	VLT
62	001.3-01.2	17:53:47.16	-28:27:17.84	Bmrs	6.2	VLT	223	009.8-04.6	18:25:05.00	-22:34:52.64	Bamrs	11.0	VLT
64	001.4+05.3	17:28:37.63	-24:51:07.16	Baps	8.6	VLT	1147	350.5-05.0	17:42:54.08	-39:36:24.29	Emrs	9.2	VLT
70	001.6-01.3	17:54:34.89	-28:12:43.62	Brs	5.4	VLT	1151	351.1+04.8	17:03:46.84	-33:29:44.64	Emrs	6.0	<i>HST</i>
73	001.7+05.7	17:28:01.74	-24:25:23.72	Eamrs	12.2	VLT	1152	351.2+05.2	17:02:19.10	-33:10:05.02	Bm	14.4	VLT
74	001.7-04.4	18:07:14.56	-29:41:24.67	Bamrs	4.6	<i>HST</i>	1156	351.6-06.2	17:50:44.60	-39:17:25.98	Bamprs	15.0	VLT
81	002.0-06.2	18:15:06.50	-30:15:32.90	Eams	6.4	VLT	1159	351.9+09.0	16:50:17.08	-30:19:55.39	Bmprs	15.4	VLT
83	002.1-02.2	17:59:19.33	-28:13:48.31	Bmrs	5.2	VLT	1160	351.9-01.9	17:33:00.68	-36:43:52.94	Bs	4.8	<i>HST</i>
82	002.1-04.2	18:07:07.28	-29:13:06.07	Bmps	8.2	<i>HST</i>	1161	352.0-04.6	17:45:06.80	-38:08:49.49	Bmp	7.4	VLT
90	002.2-09.4	18:29:11.64	-31:29:59.24	Bmprs	13.8	<i>HST</i>	1163	352.1+05.1	17:05:30.72	-32:32:08.22	Bs	18.0	VLT
91	002.3+02.2	17:42:30.02	-25:45:28.84	Eamrs	6.6	VLT	1164	352.6+03.0	17:14:42.93	-33:24:47.61	Bamprs	5.2	<i>HST</i>
93	002.3-03.4	18:04:28.81	-28:37:38.29	Bmrs	5.8	<i>HST</i>	1171	353.2-05.2	17:50:45.20	-37:23:53.09	Bmrs	16.8	VLT
98	002.5-01.7	17:58:31.20	-27:37:05.37	Ears	5.6	VLT	1172	353.3+06.3	17:04:18.33	-30:53:29.08	Bp	8.2	VLT
4326	002.6+02.1	17:43:39.48	-25:36:42.87	Bs	18.4	VLT	1178	353.7+06.3	17:05:13.91	-30:32:19.53	Bmprs	10.0	VLT
105	002.7-04.8	18:11:04.99	-28:58:59.22	Bamprs	18.2	<i>HST</i>	1185	354.5+03.3	17:18:51.94	-31:39:06.52	Bas	2.6	<i>HST</i>
106	002.8+01.7	17:45:39.80	-25:40:00.52	Bmars	4.0	<i>HST</i>	1189	354.9+03.5	17:19:20.24	-31:12:40.95	Bas	3.6	<i>HST</i>
107	002.8+01.8	17:45:28.34	-25:38:11.89	Bars	9.4	VLT	1191	355.1-06.9	18:02:32.32	-36:39:11.22	Em	9.8	VLT
109	002.9-03.9	18:08:05.76	-28:26:10.65	Bamrs	6.6	<i>HST</i>	1199	355.4-02.4	17:44:20.61	-34:06:40.96	Bms	10.6	<i>HST</i>
114	003.1+03.4	17:40:07.42	-24:25:42.77	Eamrs	4.0	<i>HST</i>	1202	355.6-02.7	17:46:06.30	-34:03:45.54	E	8.0	VLT
116	003.2-06.2	18:17:41.44	-29:08:19.88	Bps	11.0	VLT	1209	355.9+03.6	17:21:31.91	-30:20:48.75	Eam	3.8	<i>HST</i>
125	003.6+03.1	17:41:57.26	-24:11:16.33	Baps	5.8	<i>HST</i>	1207	355.9-04.2	17:52:58.94	-34:38:22.99	Bmps	8.2	<i>HST</i>
126	003.6-02.3	18:03:11.87	-26:58:32.76	Bars	10.0	VLT	1212	356.1-03.3	17:49:50.90	-34:00:31.31	Bas	5.2	<i>HST</i>
128	003.7+07.9	17:24:45.28	-21:33:34.88	Bars	11.2	VLT	1217	356.3-06.2	18:02:32.00	-35:13:13.69	Ers	11.6	VLT
129	003.7-04.6	18:12:34.39	-27:58:10.70	Ears	6.8	VLT	1219	356.5-03.6	17:51:50.60	-33:47:35.59	Bps	11.4	<i>HST</i>
131	003.8-04.3	18:11:29.26	-27:46:15.92	Baps	5.4	<i>HST</i>	1230	356.8+03.3	17:25:06.10	-29:45:16.88	Bp	3.6	<i>HST</i>
135	003.9+01.6	17:48:28.47	-24:41:23.79	Bars	8.6	VLT	1227	356.8-05.4	18:00:18.23	-34:27:40.73	Bmrs	14.4	VLT
133	003.9-02.3	18:03:39.30	-26:43:33.87	Bas	7.6	VLT	1232	356.9+04.4	17:21:04.46	-29:02:59.76	Bmps	5.8	<i>HST</i>
134	003.9-03.1	18:06:50.03	-27:06:19.58	Ears	7.8	<i>HST</i>	1234	357.0+02.4	17:28:50.35	-30:07:44.99	Ears	8.6	VLT
139	004.0-03.0	18:06:40.91	-26:54:56.28	Bamrs	6.6	<i>HST</i>	1235	357.1+03.6	17:24:34.43	-29:24:19.59	Bas	8.4	VLT
140	004.1-03.8	18:10:12.28	-27:16:35.41	Bms	3.4	<i>HST</i>	4139	357.1+04.4	17:21:37.98	-28:55:14.63	Ers	10.8	VLT
142	004.2-03.2	18:08:01.38	-26:54:02.29	Bs	6.4	VLT	1239	357.1-04.7	17:58:14.45	-33:47:37.45	Bprs	3.6	<i>HST</i>
141	004.2-04.3	18:12:25.12	-27:29:13.19	Bps	6.6	VLT	1242	357.2+02.0	17:31:08.11	-30:10:28.15	Rmrs	4.8	<i>HST</i>
143	004.2-05.9	18:18:38.34	-28:07:59.00	Bs	9.0	VLT	1246	357.3+04.0	17:23:24.94	-28:59:06.07	Ea	8.6	VLT
4315	004.3+01.8	17:48:36.54	-24:16:34.24	Bs	8.8	VLT	1252	357.5+03.1	17:27:24.36	-29:21:14.62	Ea	6.0	VLT
148	004.6+06.0	17:33:37.58	-21:46:24.80	Emrs	8.0	VLT	1253	357.5+03.2	17:26:59.83	-29:15:31.87	Bas	10.20	VLT
151	004.8+02.0	17:49:00.51	-23:42:54.90	Eas	4.0	<i>HST</i>	1256	357.6-03.3	17:53:16.81	-32:40:38.58	Bs	12.6	VLT
150	004.8-05.0	18:16:11.43	-27:14:57.98	Bars	11.4	VLT	1259	357.9-03.8	17:56:13.93	-32:37:22.21	Bmrs	13.0	VLT
156	005.0-03.9	18:12:22.99	-26:32:54.50	Eamrs	12.8	VLT	4140	357.9-05.1	18:01:22.20	-33:17:43.08	Bmps	26.4	VLT
162	005.2+05.6	17:36:22.64	-21:31:12.37	Ers	9.0	VLT	1258	358.0+09.3	17:05:44.60	-25:25:01.49	Bamprs	14.8	VLT
4106	005.5+06.1	17:35:21.32	-20:57:20.52	Bs	6.0	VLT	1263	358.2+03.5	17:27:32.87	-28:31:06.94	E	6.8	VLT
165	005.5-04.0	18:13:40.62	-26:08:39.43	Ears	12.4	VLT	1266	358.2+04.2	17:24:52.10	-28:05:54.60	Em	14.0	VLT

Table 1 – continued

HASH ID	PN G	PN Centroid Coords.		Morph.	Ang. Diam.	Tele.	HASH ID	PN G	PN Centroid Coords.		Morph.	Ang. Diam.	Tele.
		RA(J2000)	DEC(J2000)						RA(J2000)	DEC(J2000)			
1275	358.5+02.9	17:30:30.43	-28:35:54.90	Bas	3.8	<i>HST</i>	1312	359.3–01.8	17:51:18.93	-30:23:53.23	Bp	6.8	VLT
1276	358.5–04.2	17:59:02.51	-32:21:43.63	Bmps	7.8	<i>HST</i>	1319	359.6–04.8	18:04:07.75	-31:39:10.74	Brs	16.6	VLT
1280	358.6+07.8	17:12:39.17	-25:43:37.50	Bs	13.4	VLT	1322	359.7–01.8	17:52:05.97	-30:05:14.12	Ramrs	8.0	VLT
1281	358.6–05.5	18:04:56.21	-32:54:01.25	Bamps	16.8	VLT	1327	359.8+02.4	17:35:48.12	-27:43:20.40	Em	5.2	VLT
1286	358.7+05.2	17:22:28.29	-27:08:42.51	Eamrs	3.6	<i>HST</i>	1324	359.8+03.7	17:30:46.74	-27:05:59.76	Bp	7.2	VLT
1293	358.8+03.0	17:31:09.28	-28:14:50.17	Ears	8.8	VLT	1328	359.8+05.2	17:25:23.63	-26:11:53.00	Bprs	21.4	VLT
1295	358.9+03.4	17:30:02.55	-27:59:18.19	Bamps	3.2	<i>HST</i>	1329	359.8+05.6	17:24:01.48	-25:59:23.39	B	7.0	VLT
1298	359.0–04.1	17:59:56.74	-31:54:27.90	Bms	9.2	VLT	1326	359.8+06.9	17:19:13.39	-25:17:17.32	Bmps	31.8	VLT
1302	359.1–02.9	17:55:05.70	-31:12:16.85	Bs	10.0	VLT	1330	359.8–07.2	18:14:50.60	-32:36:55.30	Em	11.6	VLT
1308	359.2+04.7	17:25:44.08	-26:57:48.04	Ears	2.6	<i>HST</i>	1334	359.9–04.5	18:03:52.62	-31:17:46.79	E	9.0	VLT

and in two cases, near infrared J, H and K_s data from the VVV (Saito et al. 2012b). These measurements are summarised in Table 1 and Table 2. All centroid coordinates of PNe in this sample were re-measured with this unique set of combined high angular resolution and high sensitivity imaging data. Currently none of the VLT images have yet been ingested into HASH.

5.1 Updated angular size measurements

The new VLT imagery provides an opportunity to improve the angular size estimates currently in HASH as previously estimated from the SHS imagery. The generally better seeing in the VLT imagery c.f. the 2 arcseconds typical for the SHS, and the better VLT resolution allows improved estimation of PNe angular size. This is an important parameter when estimating kinematic age. Angular size measures are taken from the main body of the PNe and not from any very faint outer halos that likely reflect earlier mass loss off the AGB. All new angular size values are provided in Table 1 and were consistently taken from the 98% intensity plots from the VLT and *HST* fits images with histogram equalized scaling. We believe this choice better reflects the true extent of the ejected material that constitutes these PNe.

Estimated errors in angular size measurements are 4 image pixels which is 0.5 and 0.2 arcseconds for the VLT and *HST* images respectively. Comparison with current HASH values show a mean difference of 3.4 arcseconds. The average angular size of this re-measured ≤ 10 arcsecond PNe bulge sample is 9.5 with $\sigma = 5.0$. Interestingly, 47 PNe now exceed (mostly marginally) the original ≤ 10 arcsecond major diameter HASH based angular diameter selection criterion.

5.2 Morphological classification

Below we present the results from our re-evaluated morphological classifications for all 136 PNe in the bulge sample. We examine the effect of image quality, show the new distribution of morphological classes, reveal the surprising prevalence of bipolars and the incidence of point-symmetric and non-symmetric structures. This discussion supplements the PN by PN listing given in Table 1. Improved image resolution for many compact bulge PNe from the VLT (and in some cases from Pan-STARRS) together with a fresh assessment of the *HST* imagery has revealed additional morphological structures for many PNe in this sample. All PNe *HST* imagery is already in HASH and was usually used for the original HASH morphological classifications. In some cases even the true basic PNe form, not apparent from the lower resolution imagery previously used, has been revealed for the first time.

5.2.1 The effect of image quality

It is clear from this work that assigned PNe morphology, both in terms of basic classes and also sub-classifications is, unsurprisingly, a strong function of the resolution, depth and sensitivity of the available imagery especially when the PN is compact. In Fig. 4 we show two examples that demonstrate the image quality comparison between the original SHS imagery and the VLT and *HST* imagery selected from the 40 PNe where both observational data sets are available. This demonstrates the effect in going from lower to intermediate to high image resolution and how this can alter assigned morphological classifications. This is only really an issue for compact PNe in HASH with diameters < 10 arcseconds, as for our bulge sample.

In the top panel PNG 352.6+03.0 is presented. It shows a main morphology shift from class from ‘E’ to ‘B’ when going from the SHS to the VLT image. The final *HST* images at right reveal more structural details that allow for additional ‘sparm’ classifiers. The lower panel show images of PNG 008.6-02.6. The main morphological class has been changed from ‘R’ in the SHS to ‘E’ in the VLT while the *HST* image shows the PN is actually a bipolar with outer structures and internal over densities. The CSPN is now also visible. Both examples demonstrate the importance of image quality and resolution in PNe morphological classification. We note 32 of the 40 objects classified from the VLT imagery have morphological results somewhat inconsistent with their *HST* counterparts which are used in preference. This demonstrates that using images where small-scale internal and outer PN features are not well-resolved or seen can lead to basic classification errors and differences in the sub-class assignments.

5.2.2 An enrichment in bipolar morphology revealed

The revised morphological classification of the bulge PNe were compared with those recorded in the HASH database. Changes in the main and sub-classifiers are summarised in Table 3. PNe of the morphological class I and A are rare: only one was found in this sample. In HASH overall they represent a mere 0.7% and 0.4% of all Galactic PNe.

Among the 96 of 136 PNe observed with the VLT and where the pre-imaging provides the best available data, 5 now reveal an elliptical nebulosity with no resolved internal structure, resulting in a new ‘E’ class designation. They were previously classified as ‘S’ for point-like objects in HASH from the previous lower resolution optical imagery. For the remaining 91 PNe, the main “ERBIAS” morphology of 45 PNe have changed in this new assessment from their current HASH values. Some 36 PNe classified as E, R or S actually exhibit clear

Table 2. A total of 78 PNe with CSPN detected in the combined imaging data of our sample. Cols. 1-2 list HASH IDs and PN G numbers of each nebula, cols 3-4 refer to the CSPN coordinates measured in this work, telescopes used for the CSPN detection are given in col. 5, cols. 6-7 are coordinates of *Gaia* CSPN identifications. The 63 we consider to have been correctly identified in *Gaia* EDR3 are listed with "Y" in the "True?" column (col. 8). The angular separations between true CSPNe and *Gaia* identifications are listed in col. 9. Cols. 10-14 are the apparent magnitudes in *Gaia* G band, parallaxes and uncertainties in parallaxes respectively. The spectral types of 22 CSPN that were reported in Weidmann et al. (2020) are also shown in the last column. There are 3 CSPN spectra types that are indicated as being in binary systems by '+?' where the nature of the binary companion is unknown.

HASH ID	PN G	This Work		Tele.	Gaia EDR3		True?	Δr_* (arcsec)	G (mag)	ω (mas)	σ_ω (mas)	D (kpc)	Spec. Type
		RAJ2000	DECJ2000		RAJ2000	DECJ2000							
12	000.1+02.6	17:35:35.44	-27:24:05.37	VLT	17:35:35.45	-27:24:05.40	Y	0.07	17.9				
17	000.1-02.3	17:55:20.55	-29:57:36.40	VLT			New						
19	000.2-01.9	17:53:45.64	-29:43:46.98	VLT	17:53:45.65	-29:43:46.94	Y	0.13	16.9	-0.164	0.112	6.49 ^{+1.27} _{-1.16}	O(H)6-8 III-V+?
27	000.4-02.9	17:58:19.40	-30:00:39.36	VLT	17:58:19.39	-30:00:39.36	Y	0.10	18.3	0.367	0.189	4.63 ^{+1.5} _{-1.38}	
40	000.7+03.2	17:34:54.73	-26:35:57.28	PS	17:34:54.72	-26:35:57.33	Y	0.14	20.9				
38*	000.7-03.7	18:02:19.26	-30:14:25.94	VLT	18:02:19.26	-30:14:25.89	Y?	0.05	18.4	1.391	0.299	0.98 ^{+2.18} _{-0.28}	
42°	000.7-07.4	18:17:37.20	-31:56:46.87	VVV	18:17:37.20	-31:56:46.99	N	0.12					
58	001.2+02.1	17:40:12.83	-26:44:21.83	HST	17:40:12.84	-26:44:21.75	Y	0.11	18.7	-0.116	0.404	5.92 ^{+1.78} _{-1.71}	
60	001.2-03.0	18:00:37.62	-29:21:50.67	PS	18:00:37.62	-29:21:50.73	Y	0.08	15.7	0.091	0.052	8.92 ^{+2.11} _{-1.82}	[WC 11]?
62	001.3-01.2	17:53:47.17	-28:27:17.99	VLT	17:53:47.17	-28:27:18.09	Y	0.12	18.0	0.751	0.297	4.84 ^{+3.77} _{-2.84}	
73	001.7+05.7	17:28:01.74	-24:25:23.72	VLT	17:28:01.75	-24:25:23.43	N	0.32					
74*	001.7-04.4	18:07:14.56	-29:41:24.67	HST	18:07:14.56	-29:41:24.61	N	0.07					[WC 11]
90	002.2-09.4	18:29:11.64	-31:29:59.24	HST	18:29:11.65	-31:29:59.19	Y	0.09	15.2	0.276	0.086	4.57 ^{+1.24} _{-1.03}	[WO 4]pec
91	002.3+02.2	17:42:30.02	-25:45:28.84	VLT	17:42:29.90	-25:45:27	N	2.42					
93	002.3-03.4	18:04:28.81	-28:37:38.29	HST	18:04:28.81	-28:37:38.29	Y	0.05	18.9				
98	002.5-01.7	17:58:31.20	-27:37:05.37	VLT	17:58:31.22	-27:37:04.60	N	0.82					
4326	002.6+02.1	17:43:39.48	-25:36:42.87	VLT	17:43:39.55	-25:36:42.84	N	0.97					
105	002.7-04.8	18:11:04.99	-28:58:59.22	HST	18:11:04.99	-28:58:59.09	Y	0.13	18.3	-1.359	0.524	4.31 ^{+1.1} _{-1.03}	cont.
106	002.8+01.7	17:45:39.80	-25:40:00.52	HST	17:45:39.80	-25:40:00.50	Y	0.02	17.8	-0.148	0.16	11.85 ^{+3.59} _{-3.31}	
109	002.9-03.9	18:08:05.76	-28:26:10.32	HST	18:08:05.77	-28:26:10.81	N	0.51					
114	003.1+03.4	17:40:07.42	-24:25:42.77	HST	17:40:07.42	-24:25:42.67	Y	0.11	16.5	0.083	0.062	7.88 ^{+1.73} _{-1.53}	
125	003.6+03.1	17:41:57.26	-24:11:16.33	HST	17:41:57.26	-24:11:16.24	Y	0.10	17.6	-0.45	0.581	8.43 ^{+2.35} _{-2.31}	wels
129	003.7-04.6	18:12:34.39	-27:58:10.70	PS	18:12:34.39	-27:58:10.65	Y	0.06	16.9				wels
131	003.8-04.3	18:11:29.26	-27:46:15.92	HST	18:11:29.31	-27:46:16.16	N	0.69					
134	003.9-03.1	18:06:50.03	-27:06:19.58	HST	18:06:50.03	-27:06:19.51	Y	0.08	19.4				
139	004.0-03.0	18:06:40.91	-26:54:56.28	HST	18:06:40.91	-26:54:56.38	Y	0.11	14.4	0.053	0.038	9.69 ^{+1.74} _{-1.55}	O(H)f+?
142	004.2-03.2	18:08:01.39	-26:54:02.14	PS	18:08:01.39	-26:54:02.18	Y	0.04	17.2	-0.104	0.109		
141	004.2-04.3	18:12:25.11	-27:29:13.18	PS	18:12:25.11	-27:29:13.20	Y	0.04	16.4	0.283	0.082	6.10 ^{+3.21} _{-2.11}	wels
143	004.2-05.9	18:18:38.35	-28:07:58.53	VLT	18:18:38.35	-28:07:58.60	Y	0.07	17.3	0.286	0.151		
4315	004.3+01.8	17:48:36.54	-24:16:34.24	VLT	17:48:36.54	-24:16:34.23	Y	0.05	16.2	-0.024	0.142	5.73 ^{+1.28} _{-1.18}	
148	004.6+06.0	17:33:37.58	-21:46:24.80	VLT	17:33:37.58	-21:46:24.88	Y	0.08	17.6	0.048	0.15	6.41 ^{+1.65} _{-1.52}	wels
151	004.8+02.0	17:49:00.51	-23:42:54.90	HST	17:49:00.51	-23:42:54.84	Y	0.06	16.1	0.169	0.052	8.86 ^{+3.73} _{-2.64}	
150	004.8-05.0	18:16:11.44	-27:14:57.83	PS	18:16:11.44	-27:14:57.86	Y	0.04	17.8	-0.194	0.151	7.55 ^{+1.79} _{-1.65}	
156	005.0-03.9	18:12:22.99	-26:32:54.50	VLT	18:12:22.98	-26:32:54.52	Y	0.09	19.0				
162	005.2+05.6	17:36:22.65	-21:31:12.60	VLT	17:36:22.64	-21:31:12.39	N	0.25					
4106	005.5+06.1	17:35:21.43	-20:57:23.47	PS	17:35:21.43	-20:57:23.45	Y	0.02	16.6	0.014	0.095		
165	005.5-04.0	18:13:40.60	-26:08:39.53	PS	18:13:40.60	-26:08:39.60	Y	0.07	19.3	0.608	0.429		
179	006.3+03.3	17:47:33.95	-21:47:23.29	VLT	17:47:33.94	-21:47:23.29	Y	0.11	18.5	-0.022	0.246		
180	006.3+04.4	17:43:28.75	-21:09:51.77	HST	17:43:28.76	-21:09:51.68	Y	0.12	18.1	0.018	0.177		Of?
182	006.4+02.0	17:52:41.44	-22:21:57.18	HST	17:52:41.45	-22:21:57.14	Y	0.10	17.6				wels
193	007.0+06.3	17:38:11.59	-19:37:37.62	PS	17:38:11.60	-19:37:37.75	Y	0.21	15.7	0.177	0.041		
197	007.5+07.4	17:35:10.22	-18:34:20.76	PS	17:35:10.22	-18:34:20.70	Y	0.06	19.3	0.886	0.335		
198	007.6+06.9	17:37:21.99	-18:46:41.76	PS	17:37:21.99	-18:46:41.75	Y	0.03	18.6	-0.119	0.257		
200	007.8-03.7	18:17:16.03	-23:58:54.89	PS	18:17:16.03	-23:58:54.84	Y	0.06	17.1				[WC]
201	007.8-04.4	18:20:08.84	-24:15:05.39	HST	18:20:08.84	-24:15:05.36	Y	0.05	14.5	0.033	0.032	9.93 ^{+1.46} _{-1.32}	O(H)8-9 I
4111	008.2+06.8	17:38:57.37	-18:17:35.92	HST	17:38:57.37	-18:17:35.80	Y	0.12	13.6	0.05	0.029		O(H)7-8
208	008.4-03.6	18:18:23.83	-23:24:57.50	PS	18:18:23.83	-23:24:57.57	Y	0.07	17.7	0.231	0.114		
210	008.6-02.6	18:14:50.91	-22:43:55.52	HST	18:14:50.91	-22:43:55.51	Y	0.06	17.9	0.089	0.188		
217	009.4-09.8	18:44:43.16	-25:21:33.80	PS	18:44:43.15	-25:21:33.89	Y	0.14	17.5	-0.089	0.146	8.10 ^{+1.91} _{-1.79}	
223*	009.8-04.6	18:25:04.97	-22:34:52.48	PS	18:25:04.96	-22:34:52.48	Y?	0.09	18.7	3.371	0.551	0.32 ^{+0.08} _{-0.05}	[WO 2]

Table 2 – continued

HASH ID	PN G	This Work		Tele.	Gaia EDR3		True?	Δr_{\star} (arcsec)	G (mag)	ω (mas)	σ_{ω} (mas)	D (kpc)	Spec. Type
		RAJ2000	DECJ2000		RAJ2000	DECJ2000							
1151	351.1+04.8	17:03:46.84	-33:29:44.64	<i>HST</i>	17:03:46.84	-33:29:44.52	Y	0.12	16.1	0.102	0.071	$7.08^{+1.57}_{-1.4}$	wels?
1156 [◊]	351.6-06.2	17:50:44.62	-39:17:26.80	VVV	17:50:44.60	-39:17:26.64	N	0.32					
1159	351.9+09.0	16:50:17.08	-30:19:55.39	VLT	16:50:17.08	-30:19:55.28	Y	0.12	16.6	0.122	0.082	$7.49^{+1.84}_{-1.66}$	
1160	351.9-01.9	17:33:00.68	-36:43:52.94	<i>HST</i>	17:33:00.68	-36:43:52.90	Y	0.05	18.5				
1164	352.6+03.0	17:14:42.93	-33:24:47.71	<i>HST</i>			New						
1178	353.7+06.3	17:05:13.91	-30:32:19.53	VLT	17:05:13.91	-30:32:19.60	Y	0.08	17.2				O
1189	354.9+03.5	17:19:20.24	-31:12:40.95	<i>HST</i>	17:19:20.24	-31:12:40.96	Y	0.02	19.4	0.438	0.447		
1199 [#]	355.4-02.4	17:44:20.61	-34:06:40.96	<i>HST</i>	17:44:20.64	-34:06:40.80	N	0.34					
1207	355.9-04.2	17:52:58.94	-34:38:22.99	<i>HST</i>	17:52:58.94	-34:38:22.85	Y	0.14	16.3	0.197	0.08	$6.28^{+1.81}_{-1.53}$	wels
1235	357.1+03.6	17:24:34.45	-29:24:19.80	PS	17:24:34.45	-29:24:19.79	Y	0.02	16.2	0.172	0.054	$5.67^{+1.17}_{-0.99}$	wels
1242	357.2+02.0	17:31:08.11	-30:10:28.08	<i>HST</i>			New						
1246	357.3+04.0	17:23:24.93	-28:59:05.91	PS	17:23:24.93	-28:59:06.03	Y	0.13	18.7	0.007	0.254	$7.49^{+2.25}_{-2.13}$	
1252	357.5+03.1	17:27:24.36	-29:21:14.63	PS	17:27:24.36	-29:21:14.68	Y	0.06	15.2	0.093	0.037		
1256	357.6-03.3	17:53:16.82	-32:40:38.50	VLT	17:53:16.82	-32:40:38.58	Y	0.08	19.1	0.953	0.447	$5.37^{+2.99}_{-2.92}$	O(H)+?
1259	357.9-03.8	17:56:13.93	-32:37:22.21	VLT	17:56:13.93	-32:37:22.20	Y	0.05	18.7	-2.383	0.341	$8.31^{+1.75}_{-1.66}$	
1258	358.0+09.3	17:05:44.60	-25:25:01.49	VLT	17:05:44.60	-25:25:01.52	Y	0.07	17.2	0.086	0.098		
1263	358.2+03.5	17:27:32.87	-28:31:06.86	PS	17:27:32.86	-28:31:06.93	Y	0.11	19.1	-1.589	0.486	$8.98^{+2.39}_{-2.29}$	
1275	358.5+02.9	17:30:30.43	-28:35:54.90	<i>HST</i>	17:30:30.44	-28:35:54.92	Y	0.13	19.0	1.294	0.397	$10.8^{+5.02}_{-7.25}$	
1276	358.5-04.2	17:59:02.51	-32:21:43.63	<i>HST</i>	17:59:02.51	-32:21:43.50	Y	0.13	15.1	-0.447	0.242	$7.90^{+1.91}_{-1.81}$	
1280	358.6+07.8	17:12:39.17	-25:43:37.50	VLT	17:12:39.16	-25:43:37.56	Y	0.11	16.8	-0.032	0.073		
1281	358.6-05.5	18:04:56.22	-32:54:01.05	VLT	18:04:56.23	-32:54:01.08	Y	0.11	18.6	0.36	0.206	$5.33^{+1.95}_{-1.79}$	
1286	358.7+05.2	17:22:28.29	-27:08:42.51	<i>HST</i>	17:22:28.29	-27:08:42.46	Y	0.05	16.9	0.152	0.084		
1293	358.8+03.0	17:31:09.28	-28:14:50.17	VLT			New						
1308	359.2+04.7	17:25:44.08	-26:57:48.04	<i>HST</i>	17:25:44.08	-26:57:48.01	Y	0.04	15.3	0.064	0.037		
1312	359.3-01.8	17:51:18.93	-30:23:53.23	VLT	17:51:18.92	-30:23:53.18	Y	0.10	16.0	0.083	0.062	$6.92^{+1.51}_{-1.3}$	[WC 11]
1322	359.7-01.8	17:52:05.97	-30:05:14.12	VLT	17:52:05.96	-30:05:14.15	Y	0.10	17.7	0.135	0.126	$5.16^{+1.46}_{-1.25}$	
1324	359.8+03.7	17:30:46.73	-27:05:59.91	PS	17:30:46.73	-27:05:59.86	Y	0.05	18.1	0.172	0.22	$8.09^{+2.51}_{-2.42}$	
1328	359.8+05.2	17:25:23.63	-26:11:53.00	VLT	17:25:23.62	-26:11:53.00	Y	0.09	19.0	-1.284	0.353		

* These two PNe gave suspiciously low *Gaia* distances which give unfeasibly short kinematic lifetimes. See main text for caveats.

* *HST* shows two stars within the PN envelope ~ 0.2 arcseconds apart. *Gaia* cannot resolve these. The reported astrometric solution is of low quality (Goodness of fit statistic > 100).

Gaia has selected a compact nebula knot ~ 0.3 arcseconds from the actual CSPN evident in the short exposure broad-band 457M filter *HST* imagery

◊ Two examples where the VVV NIR imagery has revealed a faint CSPN within an inner oval NIR nebula ring

bipolar features in the VLT observations. For 76 PNe, we have also made changes to the secondary "sparm" classification.

All *HST* observations are accessible in HASH via a clickable icon on the main database page for each PNe. Based on assessment of the *HST* imagery we now re-classify PNG 355.9+03.6 from 'S' to 'E', PNG 001.2+02.1 and PNG 004.0-03.0 from 'E' to 'B' (the old HASH morphologies for these two were out of date). A further 11 PNe with *HST* imagery have had their 'sparm' sub-classifiers upgraded after careful examination.

We present the fraction of objects in the different main morphological classes in the histogram in Fig. 5. We include the re-assessed morphologies of this PNe sample as well as for all Galactic "True" PNe in the HASH database plotted for comparison. From Table 3, 70% of the changes made to main HASH classifications are for newly-resolved bipolar PNe. As a result, evident bipolar PN now represent the majority (68%) of bulge PNe in our sample. Interestingly, even with the old HASH classifications, the fraction of bipolar PNe in the Galactic bulge exceeds that for general Galactic disk PNe population and accounts for the largest proportion of this population. This reveals an underestimation of the actual fraction of bipolar PNe compared to what lower resolution and poorer sensitivity imaging had

indicated. For example, when bipolar lobes are not seen (too faint) or resolved (too compact), the morphology can appear to belong to class E or even S.

This 68% fraction must be a lower limit as inclination of the bipolar to the line of sight can also hide the bipolar nature of some PNe (Pollacco & Bell 1997). Indeed, the thick nebular annular ring of PNG 357.2+02.0 shown in the upper right middle panel in Fig. 6 is probably one such case. It is a very close analogue to that modelled for a bipolar inclined only 10 degrees to the line of sight as in Fig. 2 of Pollacco & Bell (1997). It is also reminiscent of the example for PN Sp 1 (PNG 329.0+01.9) presented by Mitchell et al. (2006) where additional kinematic evidence indicate we are seeing a bipolar PN pole on.

5.2.3 Resolved point-symmetric features in bipolar PNe

The fraction of PNe with a specific secondary "sparm" morphology among each main class is summarised in Table 4. With the combined VLT, *HST* and occasional Pan-STARSS observations, the number of PNe with internal structure resolved (sub-class s) doubled. The fraction of bipolar PNe in the sub-class 's' is larger than that of the

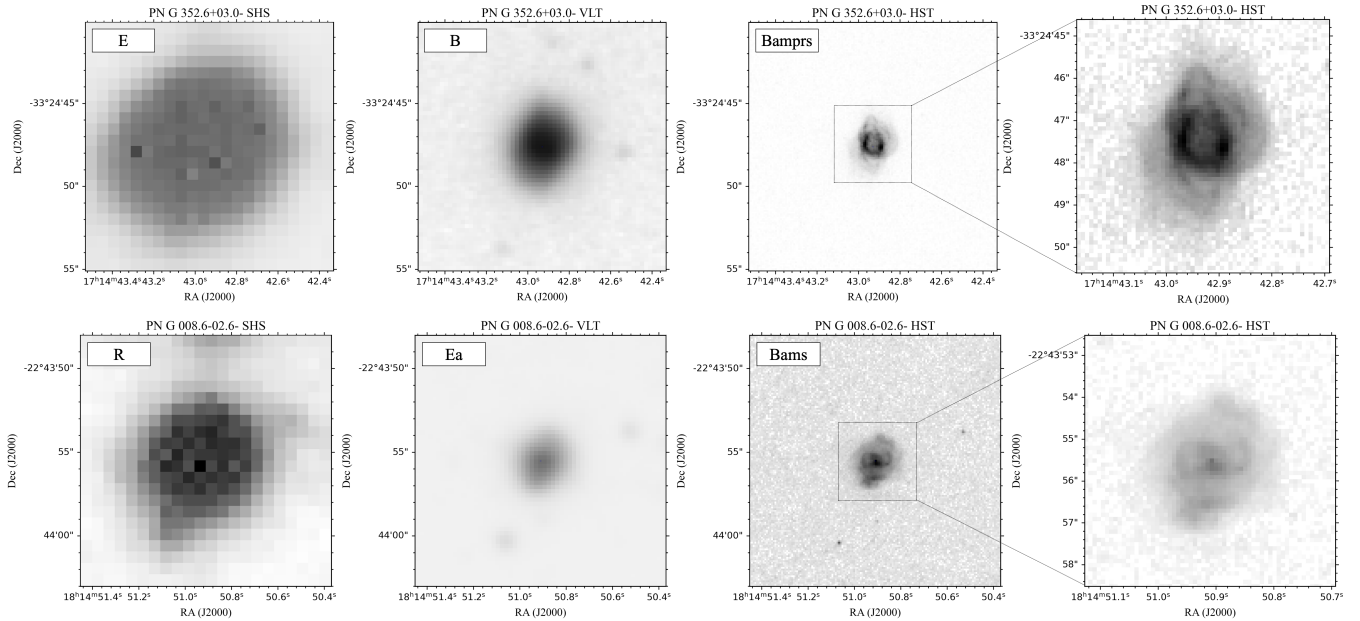


Figure 4. Two cases that contrast the difference in PN morphological classification with varying image quality. PNG 352.6+03.0 (upper panel) shows a change in morphological class assignment from ‘E’ \rightarrow ‘B’ when going from the SHS to the VLT image. The final *HST* image reveals more structural details, including the bipolar lobes and central ring structure allowing for additional ‘sparm’ classifiers to be added - better seen in the expanded, final image. The lower panel show images of PNG 008.6-02.6. The main morphological class has been changed from ‘R’ in the SHS to ‘E’ in the VLT while the *HST* image shows the PN is actually a bipolar with outer structures and internal over densities. In both cases the CSPN are also now visible thanks to *HST*.

Morphology	Change	Telescope			Total
		VLT	<i>HST</i>	PS	
Main Class	E \rightarrow B	28	2	-	30
	R \rightarrow B	4	-	-	4
	S \rightarrow B	4	-	-	4
	R \rightarrow E	6	-	1	7
	S \rightarrow E	7	1	-	8
	E \rightarrow A	1	-	-	1
Total					54
Sub-class	s	61	3	2	66
	p	16	2	-	18
	a	25	5	1	31
	r	27	3	1	31
	m	34	6	2	42
Total					188

Table 3. Improvement in PN morphological classifications possible mainly from the combined *HST* and VLT imagery. The integers show the numbers of PNe that have undergone a classification change in this study. A total of 56 PNe have had their major class changed with the bulk (38) being reclassified to bipolar for a total change of 54/136 or 70%. The bottom part of the table illustrates detection of the newly resolved sub-structures. The combined imagery allows to add 188 sub-classifiers for the whole sample (1.4 new ‘sparm’ sub-classifiers per nebula on average).

elliptical PNe, which supports the idea that determination of bipolar morphology requires better-resolved imaging. Three class ‘E’ PNe, PNG 003.6-02.3, PNG 008.4-03.6 and PNG 353.7+06.3, and one class ‘R’ PN, PNG 002.5-01.7, were observed with point-symmetric features in HASH. However, all PNe in sub-class ‘p’ in this work have bipolar morphology. There is strong observational evidence that PNe with such point-symmetric features house short-period binaries (Miszalski et al. 2009b). In our sample such features were also seen

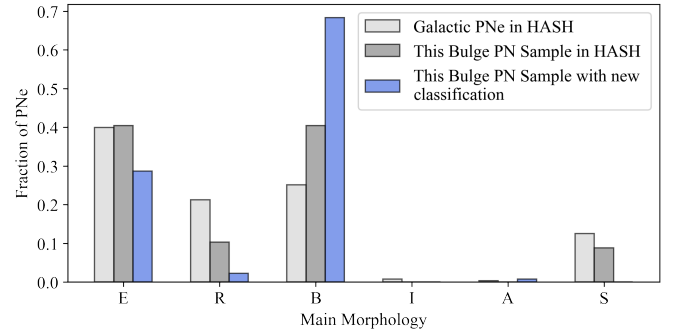


Figure 5. The fractional populations of different, basic PNe morphological classes. The blue histogram shows the sample of 136 PNe in the combined VLT and *HST* observations. The dark grey histogram indicates the previous fraction of types of this sample in the HASH database. The light grey histogram presents the fractional morphological results for all 2676 ‘True’ Galactic PNe with a morphological classification in HASH.

in PNG 002.5-01.7, PNG 003.6-02.3 and PNG 008.4-03.6 in their $H\alpha$ outer shells in catalogued images in HASH. High-resolution images of PNG 002.5-01.7 and PNG 003.6-02.3 in this combined data show no point-symmetric structure while our VLT image of PNG 008.4-03.6 exhibits clearly lobes and the equatorial concentration of matter expected for bipolar PNe, although VLT $H\alpha$ images of PNG 002.5-01.7 and PNG 003.6-02.3 are not available.

5.2.4 The incidence of non-symmetric structures

All sub-classifiers, except for sparm sub-classifier ‘a’ which describes a one-side enhancement, refer to either axisymmetrical or spherical or point-symmetrical features about the geometric centroid centre of the nebulae. The majority of PNe in this sample show morphological

Class		-	s	p	r	a	m	Total
E	HASH	19 [0.35]	13 [0.24]	3 [0.05]	15 [0.27]	22 [0.40]	14 [0.25]	55
	This Work	4 [0.10]	27 [0.69]	-	24 [0.62]	23 [0.59]	20 [0.51]	39
R	HASH	8 [0.57]	3 [0.21]	1 [0.07]	5 [0.36]	2 [0.14]	1 [0.07]	14
	This Work	-	3 [1.00]	-	2 [0.67]	3 [1.00]	2 [0.67]	3
B	HASH	14 [0.25]	34 [0.62]	16 [0.29]	17 [0.31]	8 [0.15]	19 [0.35]	55
	This Work	2 [0.02]	85 [0.91]	35 [0.38]	33 [0.35]	36 [0.39]	47 [0.51]	93

Table 4. Number of objects in a given main and sub-class for the sample of bulge PN in this work. The fraction of the total PNe of each main class is indicated in the parentheses. The upper and the lower rows compared the results in HASH and in this work.

structures with one or more of these symmetries. However, 5 PNe, PNG 002.1-02.2, PNG 008.6-02.6, PNG 354.9+03.5, PNG 356.1-03.3 and PNG 357.5+03.2, show certain structural features that are neither axisymmetrical nor point-symmetrical. Unlike a one-side protrusion or asymmetry (PNe with sub-class a) or unequal lobes that could be explained by binary interactions, such features that show a departure from axisymmetry and point-symmetry simultaneously may have resulted from the presence of a triple stellar system (e.g. Jones 2016). We do not explore this issue further in this paper.

5.3 Summary of findings for CSPN

Below we provide summary details of the main findings from our search for and identification of CSPN in our complete bulge sample.

5.3.1 Existing catalogues of CSPN and Gaia

Searching for CSPN in the overall Galactic PNe population from *Gaia* DR2 data was first conducted by González-Santamaría et al. (2019), Stanghellini et al. (2020) through a point-based matching approach, and in Chornay & Walton (2020) through an automated matching process that considered both *Gaia* relative positions and colour information. The results were updated with the latest *Gaia* EDR3 data in Chornay & Walton (2021) and González-Santamaría et al. (2021), hereafter CW21 and GSM21 respectively. A preliminary analysis by Parker et al. (2022), developed further at the WD 2022 conference in Tübingen in August 2022 by co-author Parker, indicates that the Chornay & Walton (2021) catalogue is the more reliable, but that both suffer problems of correct CSPN identification (see later). This is at least in part because many true CSPN are actually fainter than the *Gaia* limits and the bluest, most central remaining candidate gets selected instead. We compare our detected CSPN sample with those reported in CW21 and GSM21. The full CW21 sample used the entire HASH Galactic PN catalogue as the input list.

5.3.2 Comparison with existing *Gaia* CSPN listings

A quick comparison revealed that 70 of 78 CSPN recovered from our work have a nominal identification in CW21 while 71 are identified in GSM21 and 67 CSPNe appear in results of both studies for a combined total of 74 *Gaia* CSPN. Four CSPN observed, those of PNG 000.1-02.3, PNG 352.6+03.0, PNG 357.2+02.0, and PNG 358.8+03.0, were not in either of these CSPN catalogues, nor have they a *Gaia* identification, so they are newly discovered CSPN in this work. These are shown in the upper four panels of Fig. 6.

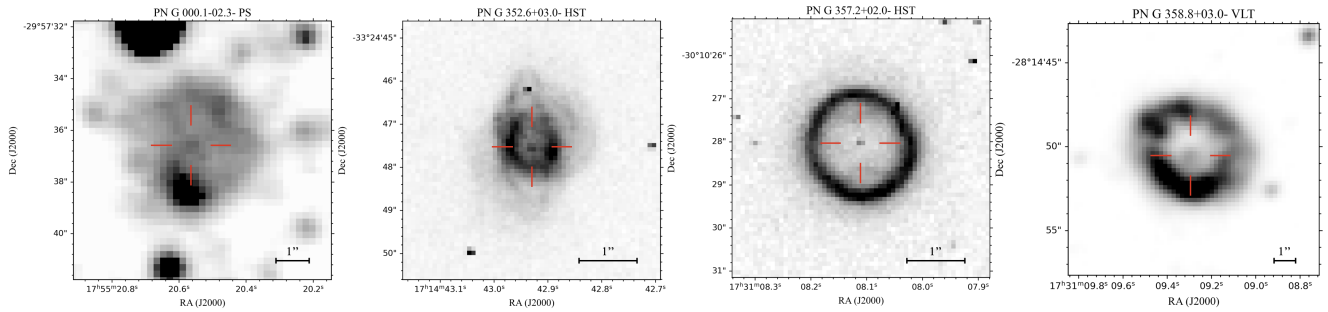
A further 11 CSPN we have identified have relatively large offsets from the stars listed as the *Gaia* CSPN in CW21/GSM21 or have other issues where we believe *Gaia* has not actually seen the true CSPN (e.g. PNG 355.4-02.4). These are false *Gaia* CSPN identifications.

They are identified with the letter 'N' in Table 2 under the column heading "True?" and comprise 14.9% of the reported *Gaia* CSPN in this sample. Four examples are shown in the lower panels of Fig. 6. In the figure the centre of the open red crosses represents the new CSPN positions while green triangles show the corresponding *Gaia* CSPN reported in CW21/CSM21. PNG 002.3+02.2 (left panel) and PNG 002.5-01.7 (left middle panel) are examples from VLT imagery where the reported *Gaia* CSPN is just part of a bright nebula region at the rim. PNG 002.9-03.9 (right middle panel) and PNG 003.8-04.3 (right panel) are examples from *HST* imagery where a brighter *Gaia* star other than the actual CSPN (which is too faint for *Gaia*) was selected. The true CSPN are fainter and bluer and both are located at the nebula's geometric centroid. There are finally two examples of CSPN identified from the VVV survey (Saito et al. 2012b) for PNG 000.7-07.4 and PNG 351.6-06.2. There is no evidence in their *HST* imagery of any visible CSPN but instead an obscured zone. We believe the reported *Gaia* CSPN merely reflects fits to the overall compact PNe and not to any true CSPN which we consider obscured by dust but visible in the NIR. The VVV imagery of both is similar - fractured oval rings surrounding a clear, faint CSPN at the centre. The optical nebula spectra of both PNe are high excitation with He II detected so there is clearly a hot star present, even if obscured. There are a further two PNe, PNG 000.7-03.7 and PNG 009.8-04.6 whose *Gaia* distances are suspiciously low. They have been assigned a Y? entry in Table 2 and are discussed in Section 5.3.4 in this paper.

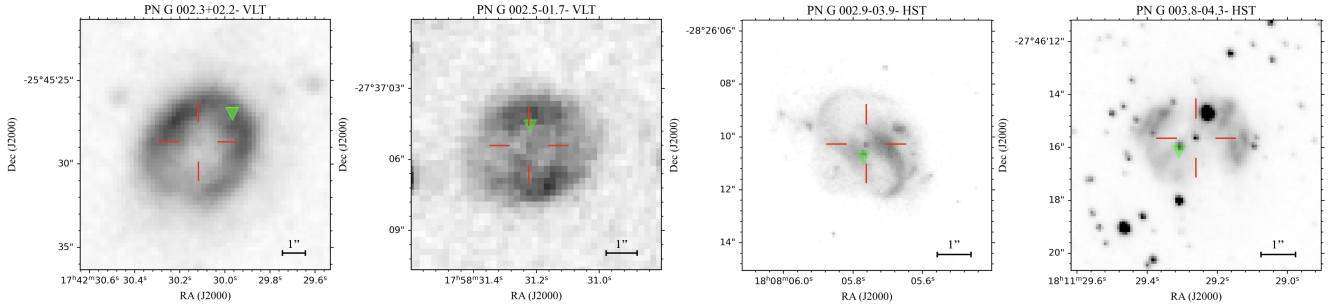
5.3.3 Issues with *Gaia* as a resource for CSPN

The *Gaia* satellite telescopes have relatively small rectangular mirrors of 1.45×0.5 m yielding a typical angular resolution never smaller than ~ 0.18 arcseconds (Lindgren et al. 2021a). In practice very few *Gaia* stars are found with separations < 0.6 arcseconds due to other limitations. Furthermore, as can be seen via the typical ground based imagery for these Bulge PNe in HASH (see Fig. 3), that without the benefit of high resolution *HST* and VLT and even Pan-STARRS image data, these largely high-surface brightness PNe appear very compact. Consequently, it is very difficult to both clearly assess the PNe morphology or actually see the CSPN, as Weidmann et al. (2020) notes. Hence, for some of the putative CSPN identified in *Gaia* for very compact PNe (e.g. for PNG 001.7-04.4), they actually likely reflect the fitted position of the compact PNe itself. This is rather than the actual resolved position and identification of the true CSPN, which in some cases are below the *Gaia* magnitude limits (Parker et al. 2022). This is even if the reported positions are sufficiently accurate as they are based on the centroid estimates of a very compact PNe.

In CW21 CSPN are attributed with a reliability factor (certainty of the CSPN identification) of between 0 and 1, and a quality label A, B or C in GSM21. These are not listed in Table 2. The reliability factor depends on the angular separation between the match and the



(a) Images of the 4 PNe with newly discovered CSPN: PNG 000.1-02.3, PNG 352.6+03.0, PNG 357.2+02.0, and PNG 358.8+03.0. The CSPN are indicated as the centres with open red crosses. The origin of the discovery image as VLT, *HST* or Pan-STARRS is given at the top with the PNG designation



(b) Examples of false *Gaia* CSPN identifications from CW21/CSM21. The open red crosses are the new CSPN positions while green triangles show the corresponding *Gaia* putative CSPN detections reported in CW21/CSM21. PNG 002.3-02.2 (left panel) and PNG 002.5-01.7 (left middle panel) are examples from VLT imagery where the reported *Gaia* CSPN is just part of a bright nebula region at the rim. PNG 002.9-03.9 (right middle panel) and PNG 003.8-04.3 (right panel) are examples (which is too faint for *Gaia*) was selected. The true CSPN are fainter and bluer and both located at the nebula's geometric centroid.

Figure 6. Upper panel: Identifications of 4 new CSPN discovered in this work. Lower panel: Examples of 4 PNe showing that the previously reported *Gaia* CSPN detections (green triangles) are false with the actual CSPN indicated via open red crosses.

position of the PN relative to the size of the nebulae and the colour. For 61 PNe with *Gaia* identifications consistent with the observed CSPN, 33 have a reliability factor > 0.85 and 26 are concluded as less-reliable with a reliability < 0.85 in CW21. When considering the reliability groups in GSM21, 11 of 15 objects with a quality label A in GSM21 show a decent match between the *Gaia* identification and with what we consider to be the actual CSPN.

The angular separations between our independently measured positions from our high resolution VLT and archival *HST* images and the reported *Gaia* CSPN coordinates in CW21 are listed in Table 2 as parameter Δr_{\star} . The values of Δr_{\star} are generally less than 10% of the major radii of the nebulae in HASH. This is followed, when available, by the astrometric measurements of parallaxes and the distance measurement in CW21.

5.3.4 CSPN parallax distances from *Gaia*

The parallax distances of 33 of the *Gaia* sources that match our CSPN observations are available. For most we consider the CSPN well determined.

For PNG 000.7-03.7 and PNG 009.8-04.6 their distances are $0.98^{+1.27}_{-0.28}$ kpc and $0.32^{+0.08}_{-0.05}$ kpc respectively. If these CSPN are correctly identified then these two PNe are in the near foreground to the bulge. However, we believe these distances are anomalous. For PNG 000.7-03.7 (HASH ID 38) the identified CSPN has a reasonable "Goodness of Fit" (GoF) statistic value (Lindgren et al. 2021b) of ~ 4 but is 0.25 arcsec from the PN's geometric centre which is unexpected for such a compact PN (angular diameter is ~ 13 arcsec-

onds). The PN is high excitation with He II λ 4686 \sim H β . In this case neither size nor spectrum are compatible with the CSPNs resultant kinematic age of 800^{+1800}_{-300} years. PNG 009.8-04.6 (HASH ID 223) has a *Gaia* GoF value of 18. Values greater than 3 are considered poor fits (Lindgren et al. 2021b). The putative CSPN is also not at the PN's geometric centre. It could even be just a dense nebula knot as it appears somewhat indistinct in the VLT imagery. The PN itself is well resolved in Pan-STARRS and has a high excitation spectrum, neither of which fits with a very low kinematic age of only 200 ± 10 years based on the identified CSPN.

If we adopt the canonical bulge distance of 8 kpc for these two PNe then the kinematic ages are 5200 and 4300 years for PNG 000.7-03.7 and PNG 009.8-04.6 respectively. This fits with expectations and our other results.

For five further PNe, PNG 002.7-04.8, PNG 002.2-09.4, PNG 000.4-02.9, PNG 357.1+03.6 and PNG 359.7-01.8, the *Gaia* sources are at $4.31^{+1.1}_{-1.03}$, $4.57^{+1.24}_{-1.03}$, $4.63^{+1.5}_{-1.38}$, $5.67^{+1.17}_{-0.99}$ and $5.16^{+1.46}_{-1.25}$ kpc, these distances are 3.4σ , 2.8σ , 2.2σ and 1.9σ smaller than 8 kpc respectively, so these five sources could possibly be PNe in the middle foreground to the bulge. Finally PNG 358.5+02.9 and PNG 002.8+01.7 have parallax distances of $10.8^{+5.02}_{-7.25}$ and $11.85^{+3.59}_{-3.31}$ kpc respectively, but still in the bulge to within the large errors. All other distances for the sample are compatible with being in the bulge.

We provide new, accurate CSPN positions for many compact bulge CSPN in this work. Our new results show that $\sim 14.9\%$ (11 out of 74 with a further two doubtful) CSPN identifications based on *Gaia* EDR3 data presented in CW21 (and GSM21) do not identify the

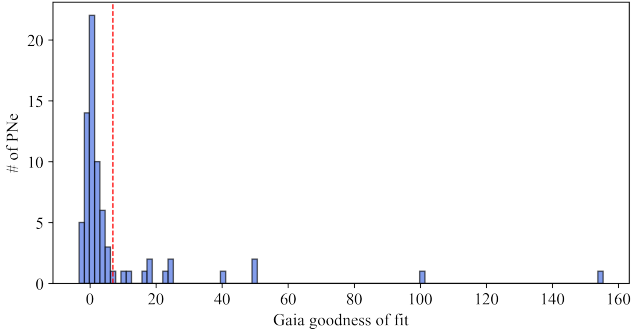


Figure 7. Distribution of available *Gaia* "Goodness of Fit" (GoF) parameter values for PNe in our sample. The red dotted vertical line is at GoF = 7, a value which includes the apparent Gaussian distribution of all but 14 of the 74 PNe with available GoF measures.

correct CSPN nor reflect the actual CSPN positions properly. As reported by Parker et al. (2022) this is a broader issue where for many PNe the true CSPN can be extremely faint and may fall below the *Gaia* limits. This may lead to the bluest star closest to the PNe geometric centroid being selected. As we are working in the dense bulge region there is usually such an alternative star choice available. Our preliminary, independent assessment of *Gaia* CSPN lists from GSM21 and CW21 for 430 checked HASH CSPN across the general Galaxy (Parker et al., in preparation), show 28% and 12% mis-identifications respectively. Correct astronomical and photometric measurements of true CSPN is vital to help understand the resultant PNe and to help ascertain their actual bulge membership when *Gaia* distances are available so care should be taken when using these compilations.

5.4 Kinematic Age Calculations

In Table 5 we present results for kinematic ages for all PNe in the sample using the best available data. This includes *Gaia* parallax distances and literature expansion velocity estimates. For 24 PNe kinematic ages are derived from the updated angular size measurements in arcseconds (from the HST, VLT and Pan-STARRS imagery) converted to a physical size in parsecs from the distances from *Gaia* data (34 cases) and literature expansion velocities in km s^{-1} (77 cases) where both are available. These are assigned quality class A. When only one of either the *Gaia* distance or literature expansion velocity are available these are assigned quality class B where a canonical bulge distance of 8 kpc is assumed if the distance is missing or an average expansion velocity of 20 km s^{-1} $\sigma = 8$ is adopted if no literature value is available. This accounts for 64 PNe in Table 5 part (b). Quality class C is where the canonical bulge distance and average expansion velocity (as calculated from all the literature expansion velocity values available in class A and B) is adopted and this covers 48 PNe. According to Gesicki et al. (2014), a correction factor of 1.4 was applied to the mass-averaged expansion velocities in the literature to account for the mean propagation speed. The errors on the kinematic ages were calculated using Monte Carlo simulations with 10,000 realizations. Lower and upper uncertainties take the 16 and 84 percentile values of the simulation estimates. The average kinematic age obtained here is 6400 ± 3800 years. The results for HASH PNe 38 and 223 are excluded from the calculations as there are serious doubts about their very low *Gaia* distances (see earlier discussion). This work represents the most accurate estimations ever provided for the kinematic ages of PNe in the Galactic bulge.

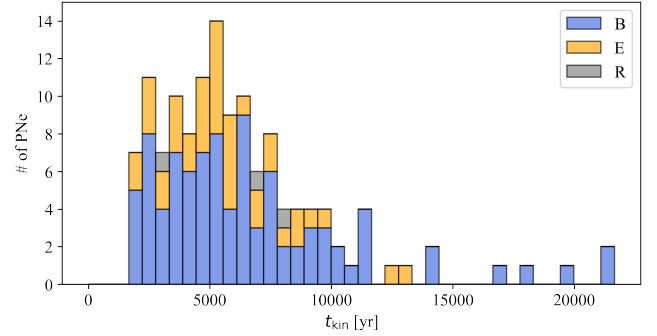


Figure 8. Distribution of kinematic ages determined for this bulge PN sample. Histograms are color-coded according to the main morphological classes.

The histogram of kinematic ages as a function of morphological type is shown in Fig. 8. The histogram bin size is about the same as the typical calculated error on the individual kinematic ages. The 7 ostensibly oldest PNe are all bipolars and they completely dominate after 10000 years with 14/16 cases. Over the range 1500 to 10000 years the fraction of ellipticals to bipolars remains approximately constant.

6 DISCUSSION

6.1 PN Morphologies and the Shaping mechanism of PNe

Round (spherical) PNe occupy a small fraction ($\sim 10\%$) in our bulge sample while the overall fraction in HASH is 21%, with many being at larger Galactic scale heights. With higher-resolution imaging more aspherical features of PNe previously classed as 'R' are found, by either revealing an elliptical outer envelope or even faint bipolar lobes. In one case, PNG 357.2+02.0, the round annular ring likely represents a bipolar PN seen pole on (refer earlier discussion in Section 5.2.2). Such "adjustments" are generally for compact PNe where significantly improved imaging resolution and sensitivity make the difference.

The generalised interacting stellar wind (GISW) model (Balick 1987), has been the cornerstone paradigm in explaining the observed aspherical features of elliptical and bipolar morphologies of PNe. Here the slow wind is enhanced in an equatorial plane expulsion of material from the progenitor post-AGB star. Under such a generalised scenario, the fast wind from the CSPN would be preferentially around an axis orthogonal to the equatorial density enhancement. A follow-up theoretical study Kahn & West (1985) conjectured that by varying the pole-to-equator density contrast in the AGB slow wind, a nebula could have a full-range of morphologies from mildly elliptical to strongly bipolar. This was substantiated by analytical models in Icke (1988), Balick (1987) and Icke et al. (1989) and later numerical simulations in Soker & Livio (1989), Mellema et al. (1991) and Icke et al. (1992).

There are also strong morphological clues as to whether a bipolar PN is likely to host a binary, e.g. Miszalski et al. (2009b). However, whether the CSPN is in a wide or close binary system cannot generally be inferred just from the PN shape (e.g. Soker 2001; Boffin & Jones 2019). The formation of bipolar lobes could be due to aspherical winds or jets and may fade on a timescale an order of magnitude smaller than the typical visibility time of a PN (Jacob et al. 2013; Gesicki et al. 2016) but see Parker (2022b).

According to best current understanding, observed PNe bipolar

Table 5. Kinematic age estimates for all PNe in the sample. For 23 PNe these are derived from the updated angular size measurements in arcseconds converted to a physical size in parsecs from the distances from *Gaia* data and literature expansion velocities in km s^{-1} . These are assigned quality class (Q) of "A". When only one of either *Gaia* distance or literature expansion velocity are available these are Q of "B" (65 PNe). A Q of "C" is where a canonical bulge distance of 8 kpc is assumed in lieu of a *Gaia* distance and an average expansion velocity of 20 km s^{-1} assumed as calculated from all the literature values available in Q of A and B (48 PNe).

(a)

HASH ID	PNG	Q	D (kpc)	R_{out} (pc)	V_{exp} (km s^{-1})	t_{kin} (yr)	HASH ID	PNG	Q	D (kpc)	R_{out} (pc)	V_{exp} (km s^{-1})	t_{kin} (yr)
19	000.2-01.9	A	$6.49^{+1.27}_{-1.16}$	0.31	$10^{[2]}$	21600^{+4700}_{-4400}	217	009.4-09.8	A	$8.10^{+1.91}_{-1.79}$	0.16	$23^{[3]}$	4800^{+1300}_{-1100}
38	000.7-03.7	A	$0.98^{+2.18}_{-0.28}$	0.03	$26^{[2]}$	800^{+1600}_{-200}	223	009.8-04.6	A	$0.32^{+0.08}_{-0.05}$	0.01	$30^{[3]}$	200 ± 000
90	002.2-09.4	A	$4.57^{+1.24}_{-1.03}$	0.15	$28^{[3]}$	3700^{+1000}_{-800}	1151	351.1+04.8	A	$7.08^{+1.57}_{-1.4}$	0.10	$23^{[1]}$	3000^{+700}_{-600}
105	002.7-04.8	A	$4.31^{+1.1}_{-1.03}$	0.19	$19^{[3]}$	6900^{+1800}_{-1700}	1159	351.9+09.0	A	$7.49^{+1.84}_{-1.66}$	0.28	$29^{[5]}$	6700^{+1600}_{-1500}
106	002.8+01.7	A	$11.85^{+3.59}_{-3.31}$	0.11	$29^{[1]}$	2600^{+700}_{-800}	1207	355.9-04.2	A	$6.28^{+1.81}_{-1.53}$	0.13	$15^{[2]}$	6000^{+1400}_{-1600}
114	003.1+03.4	A	$7.88^{+1.73}_{-1.53}$	0.07	$24^{[1]}$	2000^{+500}_{-400}	1235	357.1+03.6	A	$5.67^{+1.17}_{-0.99}$	0.11	$23^{[4]}$	3300^{+700}_{-600}
125	003.6+03.1	A	$8.43^{+2.35}_{-2.31}$	0.12	$16^{[1]}$	5200 ± 1400	1256	357.6-03.3	A	$5.37^{+2.99}_{-2.29}$	0.16	$15^{[2]}$	7400^{+4300}_{-3900}
139	004.0-03.0	A	$9.69^{+1.74}_{-1.55}$	0.16	$12^{[3]}$	9300^{+1900}_{-1600}	1263	358.2+03.5	A	$8.98^{+2.39}_{-2.29}$	0.15	$22^{[3]}$	4700 ± 1200
141	004.2-04.3	A	$6.10^{+3.21}_{-2.11}$	0.10	$18^{[3]}$	3800^{+1900}_{-1400}	1275	358.5+02.9	A	$10.8^{+5.02}_{-7.25}$	0.10	$28^{[1]}$	2400^{+1000}_{-1600}
148	004.6+06.0	A	$6.41^{+1.65}_{-1.52}$	0.12	$14^{[2]}$	5900^{+1900}_{-1300}	1276	358.5-04.2	A	$7.90^{+1.91}_{-1.81}$	0.15	$14^{[1]}$	7400^{+1900}_{-1600}
151	004.8+02.0	A	$8.86^{+3.73}_{-2.64}$	0.08	$18^{[1]}$	3100^{+1300}_{-900}	1322	359.7-01.8	A	$5.16^{+1.46}_{-1.25}$	0.10	$23^{[3]}$	3000^{+900}_{-800}
150	004.8-05.0	A	$7.55^{+1.79}_{-1.65}$	0.21	$32^{[3]}$	4500 ± 1000							

(b)

HASH ID	PNG	Q	D (kpc)	R_{out} (pc)	V_{exp} (km s^{-1})	t_{kin} (yr)	HASH ID	PNG	Q	D (kpc)	R_{out} (pc)	V_{exp} (km s^{-1})	t_{kin} (yr)
16	000.1+04.3	B	8.0 ± 1.0	0.23	$20^{[3]}$	8000^{+1200}_{-1000}	210	008.6-02.6	B	8.0 ± 1.0	0.08	$28^{[1]}$	1900^{+300}_{-200}
26	000.4-01.9	B	8.0 ± 1.0	0.16	$24^{[3]}$	4600^{+800}_{-600}	1160	351.9-01.9	B	8.0 ± 1.0	0.09	$13^{[1]}$	4800^{+900}_{-600}
27	000.4-02.9	B	$4.63^{+1.5}_{-1.38}$	0.10	20^{a}	3400^{+2500}_{-1300}	1161	352.0-04.6	B	8.0 ± 1.0	0.14	$17^{[3]}$	5700^{+1100}_{-800}
40	000.7+03.2	B	8.0 ± 1.0	0.35	$23^{[3]}$	10600^{+1400}_{-1300}	1163	352.1+05.1	B	8.0 ± 1.0	0.35	$17^{[3]}$	14300 ± 2000
37	000.7-02.7	B	8.0 ± 1.0	0.16	$27^{[3]}$	4100 ± 600	1164	352.6+03.0	B	8.0 ± 1.0	0.10	$23^{[1]}$	3000 ± 400
50	000.9-02.0	B	8.0 ± 1.0	0.10	$16^{[3]}$	4300 ± 800	1172	353.3+06.3	B	8.0 ± 1.0	0.16	$22^{[5]}$	5000^{+800}_{-700}
48	000.9-04.8	B	8.0 ± 1.0	0.30	$30^{[2]}$	6900 ± 900	1178	353.7+06.3	B	8.0 ± 1.0	0.19	$14^{[2]}$	9400^{+1600}_{-1300}
58	001.2+02.1	B	$5.92^{+1.78}_{-1.71}$	0.08	20^{a}	2700^{+2000}_{-1000}	1185	354.5+03.3	B	8.0 ± 1.0	0.05	$19^{[1]}$	1800^{+300}_{-200}
60	001.2-03.0	B	$8.92^{+2.11}_{-1.82}$	0.14	20^{a}	4800^{+3400}_{-1700}	1189	354.9+03.5	B	8.0 ± 1.0	0.07	$16^{[1]}$	3000 ± 400
62	001.3-01.2	B	$4.84^{+3.77}_{-2.84}$	0.07	20^{a}	2400^{+2900}_{-1600}	1191	355.1-06.9	B	8.0 ± 1.0	0.19	$15^{[3]}$	8800 ± 1300
73	001.7+05.7	B	8.0 ± 1.0	0.24	$39^{[3]}$	4200^{+600}_{-500}	1199	355.4-02.4	B	8.0 ± 1.0	0.21	$23^{[3]}$	6300^{+600}_{-800}
74	001.7-04.4	B	8.0 ± 1.0	0.09	$26^{[1]}$	2400^{+200}_{-300}	1202	355.6-02.7	B	8.0 ± 1.0	0.15	$11^{[3]}$	9500^{+1800}_{-1600}
81	002.0-06.2	B	8.0 ± 1.0	0.13	$7^{[3]}$	12900^{+2500}_{-2800}	1209	355.9+03.6	B	8.0 ± 1.0	0.07	$21^{[1]}$	2300 ± 300
83	002.1-02.2	B	8.0 ± 1.0	0.10	$22^{[3]}$	3100^{+400}_{-600}	1212	356.1-03.3	B	8.0 ± 1.0	0.10	$20^{[1]}$	3400^{+500}_{-400}
82	002.1-04.2	B	8.0 ± 1.0	0.16	$15^{[3]}$	7400^{+1000}_{-900}	1219	356.5-03.6	B	8.0 ± 1.0	0.22	$25^{[1]}$	6100 ± 800
91	002.3+02.2	B	8.0 ± 1.0	0.13	$17^{[3]}$	5300^{+900}_{-800}	1230	356.8+03.3	B	8.0 ± 1.0	0.07	$9^{[1]}$	5400^{+800}_{-700}
93	002.3-03.4	B	8.0 ± 1.0	0.11	$29^{[1]}$	2600 ± 300	1232	356.9+04.4	B	8.0 ± 1.0	0.11	$9^{[1]}$	8500^{+1700}_{-1100}
4326	002.6+02.1	B	8.0 ± 1.0	0.36	$41^{[3]}$	6100^{+800}_{-700}	1239	357.1-04.7	B	8.0 ± 1.0	0.07	$27^{[1]}$	1800 ± 200
109	002.9-03.9	B	8.0 ± 1.0	0.13	$39^{[1]}$	2300^{+300}_{-200}	1242	357.2+02.0	B	8.0 ± 1.0	0.09	$8^{[1]}$	7800^{+1700}_{-800}
116	003.2-06.2	B	8.0 ± 1.0	0.21	$22^{[5]}$	6600^{+1100}_{-900}	1246	357.3+04.0	B	$7.49^{+2.25}_{-2.13}$	0.15	20^{a}	5200^{+3900}_{-2000}
126	003.6-02.3	B	8.0 ± 1.0	0.20	$28^{[3]}$	4900^{+700}_{-600}	1253	357.5+03.2	B	8.0 ± 1.0	0.20	$27^{[3]}$	5100 ± 700
129	003.7-04.6	B	8.0 ± 1.0	0.13	$24^{[3]}$	3700 ± 500	1259	357.9-03.8	B	$8.31^{+1.75}_{-1.66}$	0.26	20^{a}	9000^{+6400}_{-3000}
131	003.8-04.3	B	8.0 ± 1.0	0.10	$29^{[3]}$	2400 ± 300	1281	358.6-05.5	B	$5.33^{+1.95}_{-1.79}$	0.22	20^{a}	7600^{+5900}_{-3100}
133	003.9-02.3	B	8.0 ± 1.0	0.15	$20^{[3]}$	5200^{+600}_{-800}	1286	358.7+05.2	B	8.0 ± 1.0	0.07	$22^{[1]}$	2200 ± 300
140	004.1-03.8	B	8.0 ± 1.0	0.06	$22^{[1]}$	1900^{+300}_{-200}	1293	358.8+03.0	B	8.0 ± 1.0	0.17	$20^{[2]}$	5900^{+1000}_{-700}
4315	004.3+01.8	B	$5.73^{+1.28}_{-1.18}$	0.12	20^{a}	4100^{+2700}_{-1400}	1295	358.9+03.4	B	8.0 ± 1.0	0.06	$17^{[1]}$	2400 ± 400
165	005.5-04.0	B	8.0 ± 1.0	0.24	$32^{[2]}$	5200^{+800}_{-600}	1308	359.2+04.7	B	8.0 ± 1.0	0.05	$15^{[1]}$	2300 ± 400
4108	006.1+08.3	B	8.0 ± 1.0	0.05	$16^{[1]}$	2100^{+300}_{-200}	1312	359.3-01.8	B	$6.92^{+1.51}_{-1.3}$	0.12	20^{a}	4100^{+2900}_{-1300}
180	006.3+04.4	B	8.0 ± 1.0	0.11	$46^{[1]}$	1600^{+100}_{-200}	1324	359.8+03.7	B	$8.09^{+2.51}_{-2.42}$	0.14	20^{a}	4800^{+3600}_{-1900}
182	006.4+02	B	8.0 ± 1.0	0.14	$19^{[1]}$	5100^{+700}_{-600}	1329	359.8+05.6	B	8.0 ± 1.0	0.14	$5^{[2]}$	19500^{+5200}_{-4000}
181	006.4-04.6	B	8.0 ± 1.0	0.18	$26^{[2]}$	4800^{+600}_{-700}	1330	359.8-07.2	B	8.0 ± 1.0	0.22	$29^{[5]}$	5200 ± 600
201	007.8-04.4	B	$9.93^{+1.46}_{-1.32}$	0.17	20^{a}	5900^{+4100}_{-1800}	1334	359.9-04.5	B	8.0 ± 1.0	0.17	$17^{[3]}$	6900^{+1300}_{-800}
4111	008.2+06.8	B	8.0 ± 1.0	0.09	$12^{[1]}$	5200^{+1000}_{-700}							

Table 5 – continued

(c)

HASH ID	PNG	Q	D (kpc)	R_{out} (pc)	V_{exp} (km s $^{-1}$)	t_{kin} (yr)	HASH ID	PNG	Q	D (kpc)	R_{out} (pc)	V_{exp} (km s $^{-1}$)	t_{kin} (yr)
12	000.1+02.6	C	8.0±1.0	0.24	20 ^a	8300 ⁺⁵⁵⁰⁰ ₋₂₆₀₀	192	007.0-06.8	C	8.0±1.0	0.24	20 ^a	8300 ⁺⁵⁵⁰⁰ ₋₂₅₀₀
17	000.1-02.3	C	8.0±1.0	0.20	20 ^a	6900 ⁺⁴³⁰⁰ ₋₂₂₀₀	197	007.5+07.4	C	8.0±1.0	0.35	20 ^a	12200 ⁺⁸⁰⁰⁰ ₋₃₇₀₀
20	000.2-04.6	C	8.0±1.0	0.15	20 ^a	5200 ⁺³⁵⁰⁰ ₋₁₆₀₀	198	007.6+06.9	C	8.0±1.0	0.32	20 ^a	11100 ⁺⁷⁵⁰⁰ ₋₃₄₀₀
24	000.3+06.9	C	8.0±1.0	0.21	20 ^a	7300 ⁺⁵⁰⁰⁰ ₋₂₂₀₀	200	007.8-03.7	C	8.0±1.0	0.33	20 ^a	11500 ⁺⁷⁶⁰⁰ ₋₃₄₀₀
22	000.3-04.6	C	8.0±1.0	0.23	20 ^a	8000 ⁺⁵⁴⁰⁰ ₋₂₅₀₀	208	008.4-03.6	C	8.0±1.0	0.49	20 ^a	17100 ⁺¹⁰⁹⁰⁰ ₋₅₂₀₀
42	000.7-07.4	C	8.0±1.0	0.23	20 ^a	8000 ⁺⁵¹⁰⁰ ₋₂₄₀₀	1147	350.5-05.0	C	8.0±1.0	0.18	20 ^a	6200 ⁺³⁹⁰⁰ ₋₁₉₀₀
54	001.1-01.6	C	8.0±1.0	0.15	20 ^a	5200 ⁺³⁴⁰⁰ ₋₁₆₀₀	1152	351.2+05.2	C	8.0±1.0	0.28	20 ^a	9700 ⁺⁶⁵⁰⁰ ₋₃₀₀₀
64	001.4+05.3	C	8.0±1.0	0.17	20 ^a	5900 ⁺³⁷⁰⁰ ₋₁₈₀₀	1156	351.6-06.2	C	8.0±1.0	0.29	20 ^a	10100 ⁺⁶⁷⁰⁰ ₋₃₁₀₀
70	001.6-01.3	C	8.0±1.0	0.11	20 ^a	3800 ⁺²⁶⁰⁰ ₋₁₁₀₀	1171	353.2-05.2	C	8.0±1.0	0.33	20 ^a	11500 ⁺⁷⁵⁰⁰ ₋₃₄₀₀
98	002.5-01.7	C	8.0±1.0	0.11	20 ^a	3800 ⁺²⁶⁰⁰ ₋₁₁₀₀	1217	356.3-06.2	C	8.0±1.0	0.22	20 ^a	7600 ⁺⁵¹⁰⁰ ₋₂₃₀₀
107	002.8+01.8	C	8.0±1.0	0.18	20 ^a	6200 ⁺⁴²⁰⁰ ₋₁₉₀₀	1227	356.8-05.4	C	8.0±1.0	0.28	20 ^a	9700 ⁺⁶⁴⁰⁰ ₋₂₉₀₀
128	003.7+07.9	C	8.0±1.0	0.22	20 ^a	7600 ⁺⁴⁹⁰⁰ ₋₂₁₀₀	1234	357.0+02.4	C	8.0±1.0	0.17	20 ^a	5900 ⁺⁴⁰⁰⁰ ₋₁₇₀₀
135	003.9+01.6	C	8.0±1.0	0.17	20 ^a	5900 ⁺³⁹⁰⁰ ₋₁₇₀₀	4139	357.1+04.4	C	8.0±1.0	0.21	20 ^a	7300 ⁺⁴⁷⁰⁰ ₋₂₂₀₀
134	003.9-03.1	C	8.0±1.0	0.15	20 ^a	5200 ⁺³⁶⁰⁰ ₋₁₆₀₀	1252	357.5+03.1	C	8.0±1.0	0.12	20 ^a	4100 ⁺²⁹⁰⁰ ₋₁₂₀₀
142	004.2-03.2	C	8.0±1.0	0.12	20 ^a	4100 ⁺²⁷⁰⁰ ₋₁₃₀₀	4140	357.9-05.1	C	8.0±1.0	0.51	20 ^a	17800 ⁺¹²⁰⁰⁰ ₋₅₂₀₀
143	004.2-05.9	C	8.0±1.0	0.18	20 ^a	6200 ⁺⁴⁰⁰⁰ ₋₁₈₀₀	1258	358.0+09.3	C	8.0±1.0	0.29	20 ^a	10100 ⁺⁶⁴⁰⁰ ₋₂₉₀₀
156	005.0-03.9	C	8.0±1.0	0.25	20 ^a	8700 ⁺⁵⁸⁰⁰ ₋₂₆₀₀	1266	358.2+04.2	C	8.0±1.0	0.27	20 ^a	9400 ⁺⁶²⁰⁰ ₋₂₉₀₀
162	005.2+05.6	C	8.0±1.0	0.17	20 ^a	5900 ⁺⁴¹⁰⁰ ₋₁₉₀₀	1280	358.6+07.8	C	8.0±1.0	0.26	20 ^a	9000 ⁺⁶¹⁰⁰ ₋₂₈₀₀
171	005.8-06.1	C	8.0±1.0	0.18	20 ^a	6200 ⁺⁴⁴⁰⁰ ₋₁₈₀₀	1302	359.1-02.9	C	8.0±1.0	0.19	20 ^a	6600 ⁺⁴⁶⁰⁰ ₋₂₀₀₀
179	006.3+03.3	C	8.0±1.0	0.18	20 ^a	6200 ⁺⁴⁰⁰⁰ ₋₁₉₀₀	1319	359.6-04.8	C	8.0±1.0	0.32	20 ^a	11100 ⁺⁷⁶⁰⁰ ₋₃₅₀₀
189	006.8+02.3	C	8.0±1.0	0.10	20 ^a	3400 ⁺²³⁰⁰ ₋₁₁₀₀	1327	359.8+02.4	C	8.0±1.0	0.10	20 ^a	3400 ⁺²³⁰⁰ ₋₁₀₀₀
188	006.8-03.4	C	8.0±1.0	0.14	20 ^a	4800 ⁺³¹⁰⁰ ₋₁₃₀₀	1328	359.8+05.2	C	8.0±1.0	0.41	20 ^a	14300 ⁺⁹⁵⁰⁰ ₋₄₃₀₀
193	007.0+06.3	C	8.0±1.0	0.14	20 ^a	4800 ⁺³³⁰⁰ ₋₁₅₀₀	1326	359.8+06.9	C	8.0±1.0	0.62	20 ^a	21600 ⁺¹⁴⁰⁰⁰ ₋₆₃₀₀

 References: ^[1] Gesicki et al. (2014); ^[2] Richer et al. (2010); ^[3] Richer et al. (2008); ^[4] Gesicki et al. (2006); ^[5] Gesicki & Zijlstra (2000).

^a Mean expansion velocity: 20 ± 8 km s $^{-1}$ used.

morphologies are largely due to central star binarity (e.g. Soker & Livio 1994; Boffin et al. 2012; De Marco et al. 2015; García-Segura et al. 2018; Akashi & Soker 2021; Chamandy et al. 2018), while point-symmetric structures are explained by the precession of the accretion disk around the secondary (Livio & Pringle 1996; Boffin et al. 2012).

Therefore, for cases of PNe where the shape of a bipolar waist is seen while lobes are faint or unseen, they should fit the bipolar class. Further, whether the lobes or thin rings formed in common envelope evolution (CEE) appear or not, depends largely on the kinematic age of the PN, the viewing angle and whether the internal structures are resolved. Our classification for the bipolar PNe should be more representative to this population compared with Rees & Zijlstra (2013).

6.2 Implications for the large fraction of bipolar PNe found in the Galactic bulge

The large fraction of bipolar PNe in our sample highlights not only the likely importance of binary interaction in PN shaping but raises issues of the bulge stellar population. It is also interesting to confirm that the point-symmetric features, including occurrences of multi-lobes (PNe with sub-class m and p), spiral structures or overdensities in the outer lobes are only seen in bipolar PNe and these have been strongly argued to be specific morphological traits of PNe with close binary cores (Miszalski et al. 2009b).

However, the question of why an overall ostensibly very old Galactic bulge stellar population should have a PN population highly dominated by bipolars, i.e. 68% of all compact bulge PNe known, is

important. As also known there is compelling evidence that bipolars, from Galactic disk scale height arguments alone, may also at least partially emerge from higher-mass and therefore younger progenitors, e.g. Corradi & Schwarz (1995); Parker et al. (2006) which may or may not host binaries. Another key point is the previous best estimates for the close binary fraction for PNe in the Galactic bulge is only 15-20%, where up to 60% have bipolar morphologies if the inclination effects are considered (Miszalski et al. 2009a). This compares to the lower limit bipolar fraction of 68% for all compact bulge PNe and indeed a high bipolar fraction of all bulge PNe. So do all bipolars host both more massive progenitors and binaries while close binaries in particular have additional morphological features that give them away? If so why are so many bulge PNe bipolars? If they are of higher surface brightness and so are easier to detect this does not seem to be a feature of the general Galactic disk PNe population where the apparent bipolar fraction is $\sim 20\%$ from HASH. We have shown that many compact elliptical PNe are actually bipolars in higher resolution imaging so the current HASH bipolar fraction is an underestimate but even so this cannot easily explain what we see in the Galactic bulge.

Our results for PN morphologies, therefore, suggest an underestimation of the fraction of younger and more massive stars and/or binary systems in the Galactic bulge. With a bin size of 1000 years, the number of observed bipolar and elliptical PNe start to decrease rapidly when they are kinematically older than 5000 and 6000 yr respectively in our compact sample. Taking those as estimations of typical PN life times and combining with the total PN number of 2000 in the Galactic bulge predicted in Gesicki et al. (2014) and

our results of the fractions of PN in these two morphological classes (29% for elliptical and 68% for bipolar), the birth rates of elliptical and bipolar PNe are $\sim 0.12 \text{ yr}^{-1}$ and $\sim 0.23 \text{ yr}^{-1}$ respectively. This indicates a higher, nearly doubled, death rate of progenitors of observed PNe showing bipolar morphologies.

Models show that stellar death rate decreases after the star burst and plateaus around 7 Gyr (see Fig. 10 in Gesicki et al. (2014)). Thus, if progenitors of both the elliptical and bipolar PNe are older than 7 Gyr, our PN sample should trace both populations. The higher birth rate of bipolar PNe might suggest the existence of a younger population < 7 Gyr assuming our selection criteria on the PN size leads to no morphological bias. Alternatively, the true fraction of binary systems may be much higher than expected. This is suggested by the search of binary CSPNe through the infrared (IR) excess method in (De Marco et al. 2013, 2015). Also more bipolar PNe may have been formed from long-period wide orbit binaries but that so far has limited observational evidence, or PNe might just be preferentially formed in binary systems and so are over-representing the underlying binary fraction compared with the general main-sequence population that their progenitors belong to. This is the idea of the PN *Binary Hypothesis* in De Marco (2009b). However, there are as yet no clear answers to this conundrum.

7 CONCLUSIONS

We have undertaken a detailed study of a carefully selected sample of compact PNe in the Galactic bulge. We have used our own VLT narrow-band imagery and archival narrow and broad band *HST* and occasionally Pan-STARRS broad-band imagery to provide significantly improved morphological classifications and angular size measurements for a well defined sample of compact bulge PNe. Many PNe have been re-classified as bipolars at a level that is likely to be replicated in the general HASH Galactic disk sample for PNe ≤ 10 arcseconds across, assuming deeper and higher resolution imaging eventually becomes available. The increase in the fraction of bipolar PNe comprising our bulge sample is very significant for a population ostensibly dominated by old stars. It is clear the high visibility of compact PNe allows us to find and study such a key touchstone population of late-stage stellar evolution in the Galactic bulge. If bipolars can derive from higher mass progenitors, as inferred by their preponderance at lower Galactic scale heights in the Galactic disk, as well as being in binaries, then there has to be a significant, young stellar population in the bulge feeding the observed population today. They dominate all PNe emerging from the general, several Giga year old bulge stellar population.

We have also used these data to provide a more complete and accurate listing of bulge CSPN including 4 new discoveries. We also show that 11 previous *Gaia* CSPN identified are incorrect. Many actual CSPN are beyond *Gaia* limits but visible in the deep Pan-STARRS and VLT data allowing their proper identification. For others *Gaia* has selected the wrong star or even a compact emission region as the CSPN. For some the PNe are so compact that we believe *Gaia* has simply taken the centroid of this as the CSPN given there are no other *Gaia* stars identified in the immediate region. We find for this sample that 15% of *Gaia* CSPN listed in CW21 are incorrect. As such we emphasise that great care must be taken when using the *Gaia* based CSPN compilations of CW21 and CSM21. We strongly recommend HASH (Parker et al. 2016) for such studies as every CSPN listed has been holistically vetted.

Finally, using the best available data, we provide the most complete and accurate kinematic age estimates ever compiled for all known

compact PNe in the bulge. This includes *Gaia* parallax distances for 33, accurate expansion velocities for 77, improved angular size determinations for all (from the HST, VLT and Pan-STARRS imagery) and average distance and expansion velocities for the rest. The expected young age of the PNe sample is confirmed with an average kinematic age of 6400 ± 3800 years. Kinematically older PNe are dominated by bipolars with 14/16 PNe with estimated ages > 10000 years being bipolars. Even in this compact sample these older PNe are more extended and it is easier to discern bipolar lobes. Hence a selection effect is likely at play. It is also likely that some of the very compact PNe currently classified as elliptical from the VLT imagery may turn out to be bipolars in higher resolution imagery. This would make the bipolar fraction even larger. The best current work also puts the short-period binary fraction of bulge PNe at 15-20% - maximum 60% in bipolars (Miszalski et al. 2009a), giving 9-12% of PNe in binaries are bipolars. This is a factor of up to 7 lower than the bipolar fraction we find. A younger stellar population in the bulge, wider period binaries and the relationship between PN formation and the CSPN binarity may pay a role here but the issue of the progenitor masses of the bipolar family remains. Finally, all updated angular sizes and morphological classifications presented here have also now been ingested into HASH. It is clear more work is needed to understand the observed bulge PNe morphological distribution and the associated progenitor stellar populations.

ACKNOWLEDGEMENTS

QAP thanks the Hong Kong Research Grants Council for GRF research support under grants 17326116 and 17300417. ST thanks HKU and QAP for provision of an MPhil scholarship. AR thanks HKU and QAP for the provision of a postdoctoral fellowship. AAZ acknowledges support from STFC under grant ST/T000414/1. This work has made use of data from the European Space Agency (ESA) mission *Gaia* (<https://www.cosmos.esa.int/gaia>), processed by the *Gaia* Data Processing and Analysis Consortium (DPAC, <https://www.cosmos.esa.int/web/gaia/dpac/consortium>). Funding for the DPAC has been provided by national institutions, in particular the institutions participating in the *Gaia* Multilateral Agreement.

This research made use of Astropy, a community-developed core Python package for Astronomy (Collaboration et al. 2013) and APLpy, an open-source plotting package for Python hosted at <http://aplpy.github.io>. This work used observations made with the NASA/ESA *Hubble Space Telescope*. Some data were obtained from the Hubble Legacy Archive, which is a collaboration between the Space Telescope Science Institute (STScI/NASA), the Space Telescope European Coordinating Facility (ST-ECF/ESA), and the Canadian Astronomy Data Centre (CADAC/NRC/CSA).

DATA AVAILABILITY

The data underlying this article are available in the article itself and in its associated online material freely accessible from the HASH database found here: <http://hashpn.space> by simply entering the unique HASH ID number for each source as provided.

REFERENCES

Acker A., Marcout J., Ochsenbein F., Stenholm B., Tylanda R., Schohn C., 1992, The Strasbourg-ESO Catalogue of Galactic Planetary Nebulae. Parts I, II.

Acker A., Peyaud A. E., Parker Q., 2006, Proceedings of the International Astronomical Union, 2, 355

Akashi M., Soker N., 2021, The Astrophysical Journal, 913, 91

Akras S., Gonçalves D. R., 2016, Monthly Notices of the Royal Astronomical Society, 455, 930

Ali A., Dopita M. A., Basurah H. M., Amer M. A., Alsulami R., Alruhaili A., 2016, *MNRAS*, 462, 1393

Amnuel P., 1995, Astrophysics and Space Science, 225, 275

Anderson J., King I. R., 2000, *PASP*, 112, 1360

Appenzeller I., et al., 1998, The messenger, 94

Athanassoula E., 2005, Monthly Notices of the Royal Astronomical Society, 358, 1477

Balick B., 1987, The Astronomical Journal, 94, 671

Balick B., Frank A., 2002, *ARA&A*, 40, 439

Bensby T., et al., 2013, *A&A*, 549, A147

Bensby T., et al., 2017, *A&A*, 605, A89

Blitz L., Spiegel D. N., 1991, The Astrophysical Journal, 379, 631

Boffin H. M., Jones D., 2019, The Importance of Binaries in the Formation and Evolution of Planetary Nebulae. Springer

Boffin H. M., Miszalski B., Rauch T., Jones D., Corradi R. L., Napiwotzki R., Day-Jones A. C., Köppen J., 2012, Science, 338, 773

Chamandy L., et al., 2018, Monthly Notices of the Royal Astronomical Society, 480, 1898

Chambers K. C., et al., 2016, arXiv e-prints, p. [arXiv:1612.05560](https://arxiv.org/abs/1612.05560)

Chornay N., Walton N., 2020, Astronomy & Astrophysics, 638, A103

Chornay N., Walton N., 2021, Astronomy & Astrophysics, 656, A110

Chu Y.-H., Jacoby G. H., Arendt R., 1987, *ApJS*, 64, 529

Clairmont R., Steffen W., Koning N., 2022, *MNRAS*, 516, 2711

Clyne N., Akras S., Steffen W., Redman M. P., Gonçalves D. R., Harvey E., 2015, *A&A*, 582, A60

Collaboration A., Robitaille T., Tollerud E., et al., 2013, A33

Corradi R., Schwarz H., 1995, Astronomy and Astrophysics, 293, 871

Corradi R. L. M., Schönberner D., Steffen M., Perinotto M., 2003, *MNRAS*, 340, 417

Danehkar A., Parker Q. A., Ercolano B., 2013, *MNRAS*, 434, 1513

De Marco O., 2009b, Publications of the Astronomical Society of the Pacific, 121, 316

De Marco O., 2009a, *PASP*, 121, 316

De Marco O., Passy J.-C., Frew D. J., Moe M., Jacoby G. H., 2013, Monthly Notices of the Royal Astronomical Society, 428, 2118

De Marco O., Long J., Jacoby G. H., Hillwig T., Kronberger M., Howell S. B., Reindl N., Margheim S., 2015, Monthly Notices of the Royal Astronomical Society, 448, 3587

Dwek E., et al., 1995, The Astrophysical Journal, 445, 716

Fragkou V., Parker Q. A., Zijlstra A. A., Vázquez R., Sabin L., Rechy-García J. S., 2022, *ApJ*, 935, L35

Freudling W., Romaniello M., Bramich D., Ballester P., Forchi V., García-Dabó C., Moehler S., Neeser M., 2013, Astronomy & Astrophysics, 559, A96

García-Segura G., Ricker P. M., Taam R. E., 2018, The Astrophysical Journal, 860, 19

Gesicki K., Zijlstra A. A., 2000, Astronomy and Astrophysics, 358, 1058

Gesicki K., Zijlstra A., Acker A., Górny S., Goździewski K., Walsh J., 2006, Astronomy & Astrophysics, 451, 925

Gesicki K., Zijlstra A., Hajduk M., Szyszka C., 2014, Astronomy & Astrophysics, 566, A48

Gesicki K., Zijlstra A., Morisset C., 2016, Astronomy & Astrophysics, 585, A69

González-Santamaría I., Manteiga M., Manchado A., Ulla A., Dafonte C., 2019, Astronomy & Astrophysics, 630, A150

González-Santamaría I., Manteiga M., Manchado A., Ulla A., Dafonte C., López Varela P., 2021, Astronomy & Astrophysics, 656, A51

Górny S., Stasinska G., Tylanda R., 1997, Astronomy and Astrophysics, 318, 256

Górny S., Schwarz H., Corradi R., Van Winckel H. V., 1999, Astronomy and Astrophysics Supplement Series, 136, 145

Greig W. E., 1971, *A&A*, 10, 161

Icke V., 1988, Astronomy and Astrophysics, 202, 177

Icke V., Preston H. L., Balick B., 1989, Astronomical Journal, 97, 462

Icke V., Balick B., Frank A., 1992, Astronomy and Astrophysics, 253, 224

Jacob R., Schönberner D., Steffen M., 2013, Astronomy & Astrophysics, 558, A78

Jacoby G. H., 1980, *ApJS*, 42, 1

Jones D., 2016, Proceedings of the International Astronomical Union, 12, 169

Kahn F., West K. A., 1985, Monthly Notices of the Royal Astronomical Society, 212, 837

Kaiser N., et al., 2010, in Stepp L. M., Gilmozzi R., Hall H. J., eds, Society of Photo-Optical Instrumentation Engineers (SPIE) Conference Series Vol. 7733, Ground-based and Airborne Telescopes III. p. 77330E, [doi:10.1117/12.859188](https://doi.org/10.1117/12.859188)

Kastner J. H., Moraga Baez P., Balick B., Bublitz J., Montez R., Frank A., Blackman E., 2022, *ApJ*, 927, 100

Kwitter K. B., Henry R. B. C., 2022, *PASP*, 134, 022001

Lindgren L., et al., 2021a, *A&A*, 649, A2

Lindgren L., et al., 2021b, Astronomy & Astrophysics, 649, A2

Livio M., Pringle J., 1996, The Astrophysical Journal, 465, L55

Magnier E. A., et al., 2020, *ApJS*, 251, 6

Manchado A., Villaver E., Stanghellini L., Guerrero M. A., 2000, in Kastner J. H., Soker N., Rappaport S., eds, Astronomical Society of the Pacific Conference Series Vol. 199, Asymmetrical Planetary Nebulae II: From Origins to Microstructures. p. 17 ([arXiv:astro-ph/0002073](https://arxiv.org/abs/astro-ph/0002073))

Mellema G., 1997, *A&A*, 321, L29

Mellema G., Eulderink F., Icke V., 1991, Astronomy and Astrophysics, 252, 718

Merrett H. R., et al., 2006, *MNRAS*, 369, 120

Miszalski B., Acker A., Moffat A. F., Parker Q. A., Udalski A., 2009a, Astronomy & Astrophysics, 496, 813

Miszalski B., Acker A., Parker Q. A., Moffat A. F. J., 2009b, *A&A*, 505, 249

Mitchell D. L., Pollacco D., O'Brien T., Bryce M., López J., Meaburn J., 2006, Proceedings of the International Astronomical Union, 2, 139

Nataf D. M., 2016, *Publ. Astron. Soc. Australia*, 33, e023

Nicklas H., Seifert W., Boehnhardt H., Kiese-wetter-Koebinger S., Rupprecht G., 1997, in Ardeberg A. L., ed., Society of Photo-Optical Instrumentation Engineers (SPIE) Conference Series Vol. 2871, Optical Telescopes of Today and Tomorrow. pp 1222–1230, [doi:10.1117/12.269011](https://doi.org/10.1117/12.269011)

Parker Q. A., 2022a, *Frontiers in Astronomy and Space Sciences*, 9, 895287

Parker Q. A., 2022b, *Frontiers in Astronomy and Space Sciences*, 9, 895287

Parker Q. A., et al., 2005, *MNRAS*, 362, 689

Parker Q. A., et al., 2006, *MNRAS*, 373, 79

Parker Q. A., Bojičić I. S., Frew D. J., 2016, in Journal of Physics: Conference Series. p. 032008

Parker Q. A., Xiang Z., Ritter A., 2022, *Galaxies*, 10, 32

Peimbert M., 1978, in Symposium-International Astronomical Union. pp 215–224

Peimbert M., Torres-Peimbert S., 1983, in Symposium-International Astronomical Union. pp 233–242

Phillips J. P., 2001, *MNRAS*, 326, 1041

Pollacco D. L., Bell S. A., 1997, *MNRAS*, 284, 32

Rees B., Zijlstra A., 2013, Monthly Notices of the Royal Astronomical Society, 435, 975

Reid W. A., Parker Q. A., 2006, *MNRAS*, 373, 521

Richer M. G., López J. A., Pereyra M., Riesgo H., García-Díaz M. T., Báez S.-H., 2008, The Astrophysical Journal, 689, 203

Richer M. G., López J. A., García-Díaz M. T., Clark D. M., Pereyra M., Díaz-Méndez E., 2010, The Astrophysical Journal, 716, 857

Sabin L., Zijlstra A. A., Greaves J. S., 2007, *MNRAS*, 376, 378

Sabin L., et al., 2014, Monthly Notices of the Royal Astronomical Society, 443, 3388

Sabin L., et al., 2021, Monthly Notices of the Royal Astronomical Society, 508, 1599

- Sahai R., Morris M. R., Villar G. G., 2011a, *AJ*, **141**, 134
- Sahai R., Morris M. R., Villar G. G., 2011b, *The Astronomical Journal*, **141**, 134
- Saito R. K., Zoccali M., McWilliam A., Minniti D., Gonzalez O. A., Hill V., 2011, *The Astronomical Journal*, **142**, 76
- Saito R. K., et al., 2012a, *Astronomy & Astrophysics*, **537**, A107
- Saito R. K., et al., 2012b, *A&A*, **537**, A107
- Schönberner D., Jacob R., Steffen M., Sandin C., 2007, *A&A*, **473**, 467
- Siódmiak N., Tyłenda R., 2001, *Astronomy & Astrophysics*, **373**, 1032
- Soker N., 1998, *ApJ*, **496**, 833
- Soker N., 2001, *The Astrophysical Journal*, **558**, 157
- Soker N., Livio M., 1989, *The Astrophysical Journal*, **339**, 268
- Soker N., Livio M., 1994, *The Astrophysical Journal*, **421**, 219
- Stanek K., Udalski A., Szymański M., Kałużny J., Kubiak Z. M., Mateo M., Krzemiński W., 1997, *The Astrophysical Journal*, **477**, 163
- Stanghellini L., Corradi R. L., Schwarz H. E., 1993, *Astronomy and astrophysics*, **279**, 521
- Stanghellini L., Villaver E., Manchado A., Guerrero M. A., 2002b, *The Astrophysical Journal*, **576**, 285
- Stanghellini L., Villaver E., Manchado A., Guerrero M. A., 2002a, *ApJ*, **576**, 285
- Stanghellini L., Shaw R. A., Villaver E., 2016, *The Astrophysical Journal*, **830**, 33
- Stanghellini L., Bucciarelli B., Lattanzi M. G., Morbidelli R., 2020, *The Astrophysical Journal*, **889**, 21
- Steffen W., López J. A., 2006, *Rev. Mex. Astron. Astrofis.*, **42**, 99
- Wareing C. J., Zijlstra A. A., O'Brien T. J., 2007, *MNRAS*, **382**, 1233
- Wegg C., Gerhard O., 2013, *Monthly Notices of the Royal Astronomical Society*, **435**, 1874
- Weidmann W., et al., 2018, *A&A*, **614**, A135
- Weidmann W. A., et al., 2020, *Astronomy & Astrophysics*, **640**, A10
- Zhang C. Y., Kwok S., 1998, *ApJS*, **117**, 341
- Zoccali M., et al., 2014, *Astronomy & Astrophysics*, **562**, A66

Table A1. Observing log of the VLT PNe imagery. Provided are PNG ID, narrow-band filter used, exposure time in seconds date of observation, official ESO observing program ID and the reported seeing in arcseconds (complete table is available online).

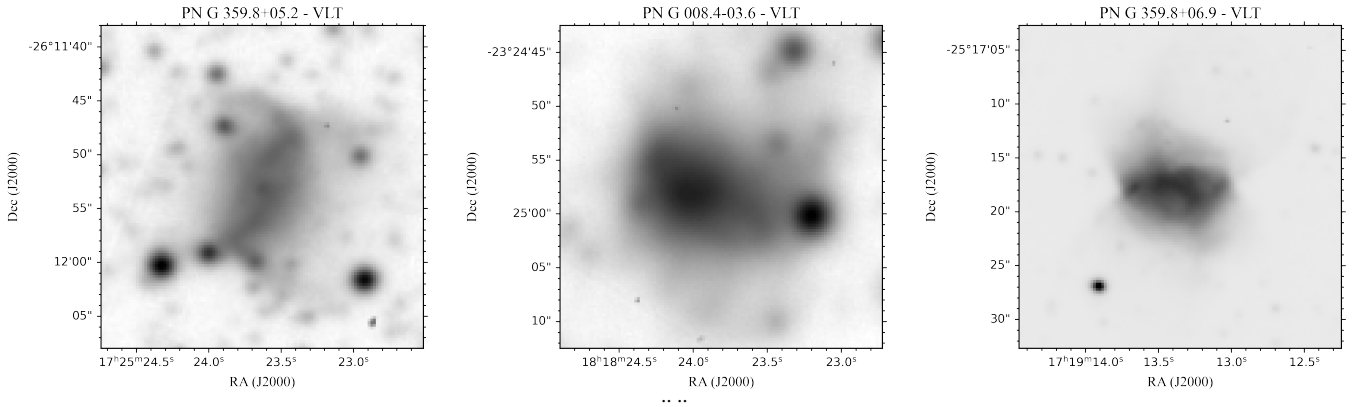
PNG	Filter	Exposure	Date	Prog. ID	Seeing
PNG 000.1+02.6	[O III]	6.0	2015-04-17	095.D-0270(A)	0.62
PNG 000.1+04.3	[O III]	10.0	2015-04-18	095.D-0270(A)	1.23
PNG 000.1-02.3	[O III]	5.0	2015-04-17	095.D-0270(A)	1.16
PNG 000.2-01.9	H α	5.0	2015-04-17	095.D-0270(A)	0.63
PNG 000.2-04.6	[O III]	5.0	2015-04-17	095.D-0270(A)	0.76
PNG 000.3+06.9	[O III]	6.0	2015-04-19	095.D-0270(A)	1.06
PNG 000.3-04.6	[O III]	5.0	2015-04-18	095.D-0270(A)	1.32
PNG 000.4-01.9	H α	5.0	2015-04-18	095.D-0270(A)	1.07
PNG 000.4-02.9	H α	4.0	2015-04-19	095.D-0270(A)	0.83
PNG 000.7+03.2	H α	5.0	2015-04-19	095.D-0270(A)	0.83
..
..

Table A2. Observing logs of the *HST* imagery used. Provided are the PN usual names or PNG IDs, the *HST* narrow band filters used to make our measurements, the exposure time in seconds, date of observation, program ID and data set (complete table is available online).

Objects	Filter	Exposure	Date	Prog. ID	Data Set
M1-42	F502N	0.5	2009-04-22	11185	ua2o010dm
M1-42	F656N	0.5	2009-04-22	11185	ua2o010bm
M1-42	F502N	600.0	2009-04-22	11185	ua2o010am
M1-42	F656N	300.0	2009-04-22	11185	ua2o0108m
M1-42-REPEAT	F502N	600.0	2009-06-09	11185	ua2o1008m
M1-42-REPEAT	F656N	300.0	2009-06-09	11185	ua2o1006m
PK002-04D1	F656N	20.0	2000-02-17	8345	u5hh4101r
PK002-04D1	F656N	140.0	2000-02-17	8345	u5hh4102r
PK002-04D1	F656N	400.0	2000-02-17	8345	u5hh4103r
PK002-09D1	F656N	230.0	2000-08-26	8345	u5hh5602r
..
..

Figure B1. The best optical PN images from the VLT or *HST* (narrow-band) and in a few cases, Pan-STARRS (broad-band) used in this study. The data origin is given at the top of each image along with the PNG ID. Images are generally that obtained with H α filters or otherwise indicated. Pan-STARRS images are in g-band, where used. Complete set of PN images is available online.

(a) PNe with angular sizes greater than 20 arcsec. Each image has a field of view of 30" \times 30".



APPENDIX A: OBSERVING LOGS FOR THE VLT (TABLE A1) AND *HST* (TABLE A2) IMAGERY USED

APPENDIX B: THE BEST OPTICAL PNE IMAGES.

This paper has been typeset from a $\text{\TeX}/\text{\LaTeX}$ file prepared by the author.